

This report is the first design report of HyPower Bristol's 2025 design cycle. This design cycle seeks to build upon and refine the work completed in the Project Feynman era.

## 1. Introduction

### 1.1 Project Objectives

- I. Following the previous developments of the HyPower Bristol team, the present design cycle will optimise and develop our systems with a *Test to Inform* objective.
- II. To combine our composite manufacture with a metallic skeleton structure to house our feed systems.
- III. To demonstrate reliable high-altitude avionics, that have the capability to control the launch of a bipropellant liquid engine.

### 1.2 Mission Objectives

- I. To remotely fuel nitrogen and nitrous oxide into our rocket on the pad from a ground station controlled by point-to-point WiFi linked to mission control.
- II. To fly a bipropellant liquid rocket on a 5kN engine to an apogee of 3km.
- III. To use a forward integration control system, and gear-driven petal air brakes to secure our accuracy on apogee.
- IV. To sample atmospheric data in the plume of the launch vehicle, by deploying a payload from the launch vehicle.
- V. To successfully recover the vehicle in a re-flyable state using a single separation, dual deployment method.

### 1.3 Mission Concept of Operations

The operations are planned as follows; firstly, to secure the rocket onto the launch rail, ensuring it is properly aligned and stable. We will then connect the fuel lines to the rocket and begin fuelling the ethanol tank. All personnel will then move away from the vehicle and the remote fuelling operations can then commence. The nitrogen and then the nitrous oxide tank will be fuelled. The quick disconnects will be released and all systems will be checked for launch. The ignition sequence will then commence, and launch will occur. During the thrust phase, instrumentation will monitor the operating chamber pressure of the engine. Once the 5s burn has finished, the vent procedure will begin. The coast phase will then use the airbrake solver to predict the apogee, and the airbrakes will be actuated to ensure accuracy. At apogee the pyro charges will fire, and the separation event will occur to release the drogue parachute along with the bagged main. At 300m, the tender descender will fire, releasing the main parachute to ensure a safe and soft landing. Upon detecting landing, the system will be recovered.

7: Apogee target at 3000m. Airbrakes stowed.

6: Forward interpolation to apogee, airbrake deployment.

5. Coast Phase: control system begins, venting of propellant.

4. Thrust Phase: 5s burn of 5kN engine.

2. Quick Disconnection – remote operation

1. Remote fueling operations

- 8. PYRO EVENT 2: Ejection charge for single separation at apogee (zero acceleration).

9. Decent at 18m/s under drogue on a riser.

- 10. PYRO EVENT 3: Tender descender ejection charge for main deployment (300m)

11. Main deployment at 350m.

12. Decent at 8m/s under main.

13. Landing of rocket.

## HyPower Bristol ConOps EuRoC'24 L3

### Hold Points:

- Pressures, and fueling duration to be nominal.
- Visual verification of Quick Disconnection
- Apogee to always be interpolated with intention of 3000m
- Ejection charge for drogue must happen at apogee
- Tender descender to release main.
- System to vent before personnel approach landed rocket.
- Rocket to be inspected and decommissioned.



Aspect	Value	Unit
Length	3450	mm
External diameter	200	mm
Apogee	3000	m
Maximum velocity		m/s
Maximum acceleration		m/s <sup>2</sup>
Nominal thrust	5000	N
Burn duration	5.5	s
Wet mass		kg
Dry mass		kg
Propellants	N <sub>2</sub> O, C <sub>2</sub> H <sub>5</sub> OH, H <sub>2</sub> O	[--]
Pressurant	N <sub>2</sub>	[--]

#### 1 – Nose & Recovery

#### 2 – Payload bay

#### 3 – Airbrake module

#### 4 – Avionics

#### 6 – Coaxial propellant tanks

#### 7 – Fin Can

#### 9 – Engine

The engine developed by BSEP is a fully regenerative design, and to be printed from CP-1 Aluminium. This will provide 5 kN of thrust for a 5.5 s burn duration, lifting the rocket to 3000 m in 25.7 s

Figure 1: Launch vehicle overview

# Systems engineering study of the launch vehicle

Requirements for success - maximum mass, minimum thrust etc

Predicted launch profile – velocity, height, time, rail velocity etc

## Definition of the engineering problem/constraints

+ hot fire data in the context of flight

## What are the failure modes of the system?

And how do we mitigate?

Mass log - Please could you add your part to this list!

### 3. Propulsion System

Do we need a summary of prop here?

#### 3.1 Combustion Chamber

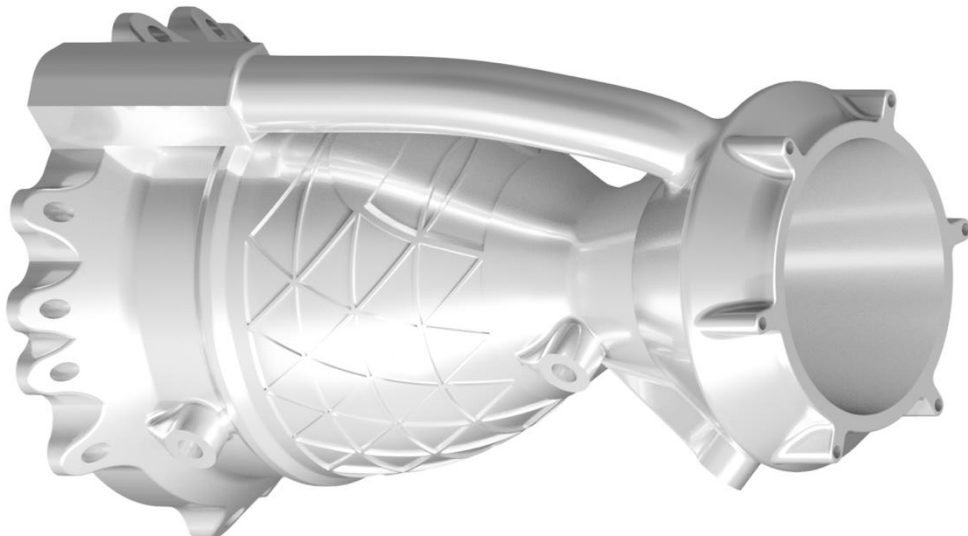


Figure 2, CAD render of the Aluminium 2025 engine.

The combustion chamber was designed as a lightweight flight version of last year's engine. The shift from Inconel 718 to CP1 Aluminium will reduce the weight threefold as well as increasing the cooling capabilities with an enhanced thermal conductivity.

The main chamber part consists of a fuel inlet tube, a fuel manifold, and a series of cooling channels for regenerative cooling. The fuel inlet tube is tapped to take a BSPP fitting, to allow integration into the full system. Multiple thermocouple ports are built into the chamber and pressure transducer ports are built into the injector to allow collection of sensor data. A weight-saving Isogrid structure was also added to the exterior wall but this feature remains in its early design phase.

##### 3.1.1. Overview of design point of engine:

Table 1: Key engine details

Property	Value
Engine type	Bi-propellant
Fuel	IPA (15% film cooling) + 1% PDMS
Oxidiser	N <sub>2</sub> O
Chamber pressure	20 bar
Thrust	5 kN
Cooling	Regenerative cooling, film cooling, additive cooling

Further details:

Table 2: Further particular details for engine design.

Property	Value	Unit
Fuel mass flow rate	0.64	kg/s
Oxidiser mass flow rate	1.93	kg/s
OF ratio	3	[--]
Chamber diameter	119.6	mm
Engine length	274.35	mm
Contraction ratio	6	[--]
Throat diameter	48.54	mm
Nozzle diameter	88.6	mm
L*	843.21	mm
Expansion ratio	3.36	[--]
Inner wall thickness	0.8	mm
Outer wall thickness	2	mm

### 3.1.2. Material Properties

The combustion chamber is to be 3D printed out of a single heat-treated piece of CP1 Aluminium, an Aluminium-Iron-Zirconium powder alloy for additive manufacture that is faster and easier to print (greater overhangs), lighter and has superior thermal conductivity to Inconel and higher high temperature performance than other alloys such as AlMgSi<sub>10</sub>. [2]

The tabulated material properties are taken from datasheets from the powder manufacturer Constellium and the printing company MTC.

Table 43: Material properties of CP1 Aluminium

Property	Value	Units
Melting Point	~900	K
Maximum Operating Temp (MOT)	577	K
Ultimate Tensile Strength	342	MPa
Yield Tensile Strength	323	MPa
Yield Strength at MOT	~85	MPa
Thermal Conductivity	187	W/m-k
Thermal Conductivity at MOT	208	W/m-k
Young's Modulus	71	GPa
Poisson Ratio	0.31	[--]
Thermal Expansion Coefficient	25.19e-6	C <sup>-1</sup>

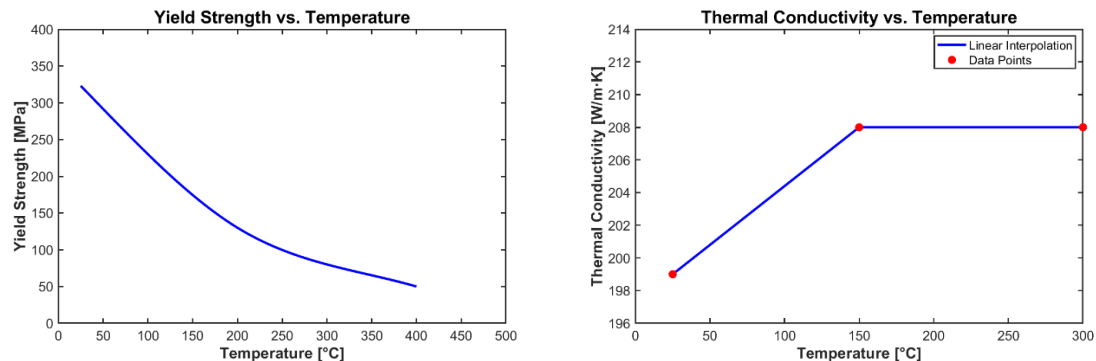


Figure 3, Yield Strength data provided by Constellium(left), Thermal conductivity data collected by the MTC (right)

As seen in the graphs above, the yield strength of CP1 fall off quite hard with temperature. This is something that must accounted for in any stress calculations and why the peak temperature should be designed to stay below 650K. The thermal conductivity increases with temperature and level off around 208W/mK<sup>2</sup> so this is the value chosen for later simulations.

More information will be provided by the MTC on heat treatment plans and more in depth material data to refine the accuracy of the models below.

### 3.1.3. Stress calculations

A series of analytical and computational simulations were performed to validate the stress experienced by each part of the system.

#### Hoop Stresses

A series of cases where look at to determine the hoop stresses experienced by the engine. This test allows us to verify that the chamber and cooling channel walls will not burst under the pressures they will be subjected to.

##### *Thick-Walled Hoop Stress*

$$\sigma_{\theta} = \frac{P_a a^2 - P_b b^2}{b^2 - a^2} + \frac{a^2 b^2 (P_a - P_b)}{(b^2 - a^2) r^2}$$

Lame's equation for thick-walled hoop stress where  $\sigma_{\theta}$  is the hoop stress,  $P_a$  is the pressure at the inner surface,  $P_b$  is the pressure at the outer surface,  $a$  is the inner diameter,  $b$  is the outer diameter, and  $r$  is the diameter inside the hoop at which the hoop stress is measured. [3]

Multiple cases were tested with different combinations of the 20 bar chamber pressure, 30 bar coolant pressure and 1atm exterior pressure at different thicknesses of the material and point of the engine.

Table 104: Results for hoop stress calculations.

Position	Analytical Value [MPa]	Safety Factor
Chamber – Channel	77.8	4.1
Chamber - Wall	24.4	13.1
Throat – channel	33.8	9.5
Throat – wall	10.5	30.5

Thin wall hoop stress was also used and found to give similar values.

#### Thermal Stresses

Multiple types of thermal stress equations were used as seen below to ensure no cracks or “doghouse effect,” which will be described later, occur. Most of the equations were taken from Stephen D. Heister’s “Rocket Propulsion.”

##### *Tangential Thermal Stress*

Two equations were used to determine the tangential thermal stress.

$$\sigma_{t1} = \frac{(P_{co} - P_g)D}{2t} + \frac{E\alpha qt}{2(1-\nu)k}$$

$$\sigma_{t2} = \frac{(P_{co} - P_g)}{2} \left(\frac{w}{t}\right)^2 + \frac{E\alpha qt}{2(1-\nu)k}$$

Where  $\sigma_t$  is the tangential stress,  $P_{co}$  is the coolant pressure,  $P_g$  is the combustion gas pressure,  $D$  is the chamber diameter,  $t$  is the inner wall thickness,  $E$  is the Young's Modulus,  $\alpha$  is the thermal expansion coefficient,  $\nu$  is the Poisson's ratio,  $k$  is the thermal conductivity, and  $w$  is the internal width of the cooling channel. [3] Tangential stresses are created by the internal pressure in the coolant passage and its relationship to the local gas pressure as well as due to thermal growth of the material on the heated side of the passage. The first half of both equations takes into account the hoop stresses, the first equation calculating it for the inner wall and the second for the channels. The second half of the equations is the tangential thermal stress induced by the heat transfer.

#### *Longitudinal Thermal Stress*

$$\sigma_l = E\alpha(T_w - T_{ow})$$

Where  $\sigma_l$  is the longitudinal stress,  $T_w$  is the hot wall temperature, and  $T_{ow}$  is the cold wall temperature. [3] The longitudinal stresses result from the tendency of the heated side of the passages to grow in length. Due to the superior ductility and thermal conductivity of CP1, the likelihood of failure from these stresses is quite low.

#### *Thermal Buckling Stress*

$$\sigma_b = \frac{EE_c \frac{t}{D}}{\left(\sqrt{E} + \sqrt{E_c}\right)^2 \sqrt{3(1-\nu^2)}}$$

Where  $\sigma_b$  is the buckling stress and  $E_c$  is the compression modulus. [3] For Aluminium the compression modulus is equal to the Young's Modulus.

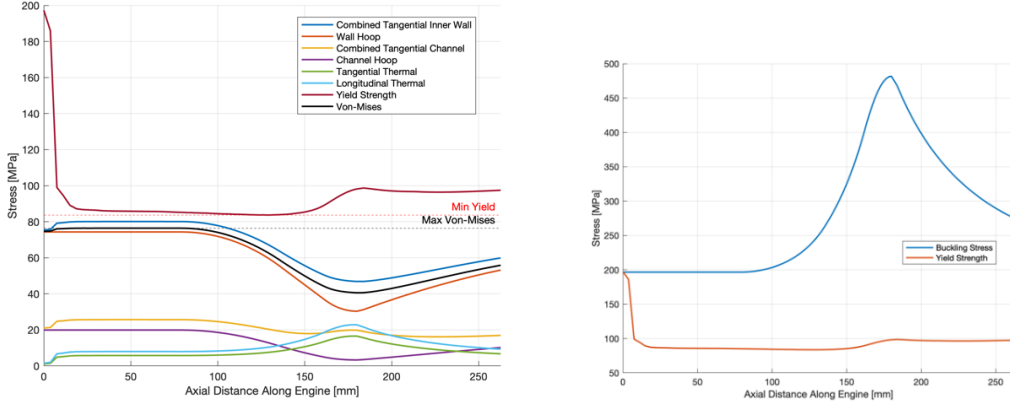


Figure 4, calculated stresses experienced by the chamber under pressure and thermal loads(left) and buckling stress (right)

The above graphs show the stress results at the every points along the engine contour. The tangential stresses were split into their hoop and thermal parts as well as combined. The yield strength values was extrapolated from the graph in the previous section to accurately model when the will yield in a given location at the operating temperature that location will experience. It can be seen from the left graph that all stresses remain below the local yield strength, hence the engine will survive these stresses at steady-state. The right graph shows that buckling stress remains comfortably above the buckling stress throughout the engine, which is ideal since if yield strength is over the buckling stress at any point, that point will buckling.

Some engine designer opt not to model the wall hoop stresses due to the inner wall being reinforced by the channel ribs, thus only modelling the pressures the channels experience themselves. This would approach would therefore reduce the maximum stress from ~80MPa to ~30MPa and would no longer be dominated by hoop stresses at the chamber, instead by longitudinal thermal stresses at the throat.

## FEA

A series of FEA models were completed to further model any potential failure points.

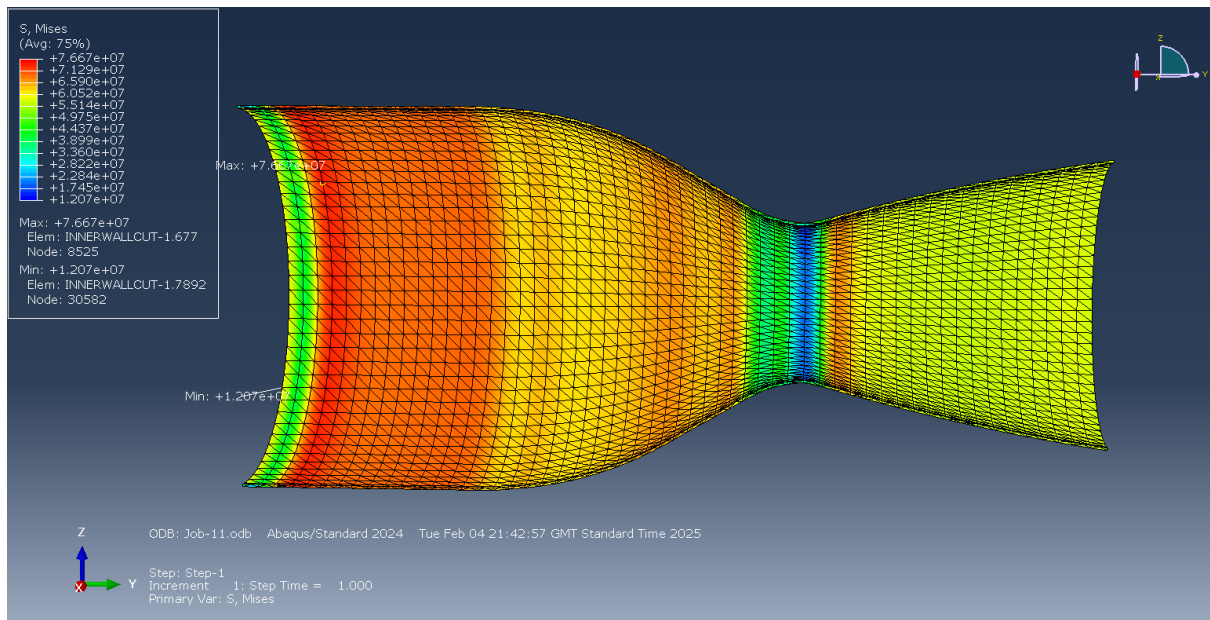


Figure 5, Abaqus FEA simulation of hoop stresses on the chamber

The simulation above consisted of a simplified version of the engine geometry, isolating the inner wall. The expected 20bar chamber pressure was applied to the inner surface and a 30bar was applied to the outer surface to act as the inwards acting pressure of the channel coolant. As seen above, the maximum stress of 76.7MPa occurred at the chamber and the stress reduced heavily at the throat. This lines up near perfectly with the results from the previous equations, with 77.8MPa equated from this case from the thick walled hoop stress equations and 74.3MPa equated from the pressure component of the inner wall tangential stress. This is the first step in validating the models and further analysis will be undertaken.

#### *Stress considerations*

The above simulations offer a worst-case scenario of the performance of the combustion chamber. Considerations should be made for the fact a list of positive factors have not been included in this modelling due to the difficulties involved in integrating these features. These factors which will act to positively affect the stress loads are as follows:

- Thermal equilibrium may not be reached with a 5s burn time; temperatures will be lower than at thermal equilibrium.
- The Bartz equation has been used which is known to overestimate when compared to other sources such as the Ievlev equation and truth data.
- Material properties of CP-1 Aluminium vary at high temperatures so the assumed Yield Strength may not be exact although attempts were made to model it. More research and testing will be done to better characterize this change in YS.
- Addition of 1% Polydimethylsiloxane (PDMS) to the fuel will act to considerably decrease wall temperatures at hotspots such as the throat as will be discussed in the next section.

### 3.1.4. Thermal Analysis

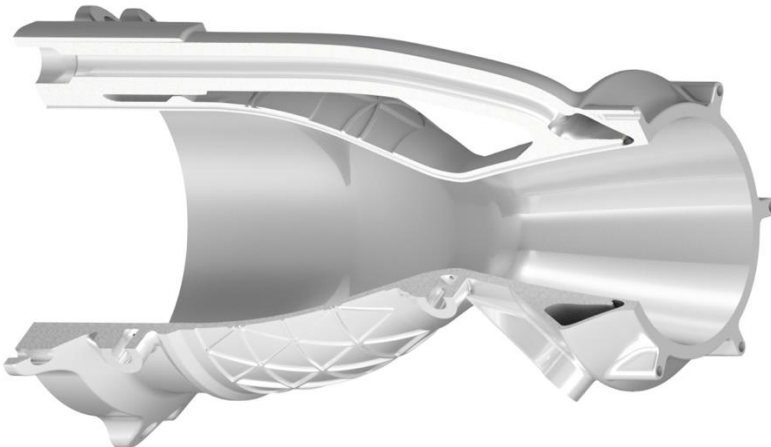


Figure 6:  $\frac{3}{4}$  view CAD render of the Aluminium 2025 engine.

### Thermal Management Design

To define the cooling solution a series of requirements were first imposed. The combustion chamber will be constructed out of the aluminium alloy ‘Aheadd® CP1 20/63’ due to its improved thermal conductivity and reduced density relative to the previous manufactured Inconel 718 engine. Minimum cooling channel dimensions would be 1.5mm to avoid any issues in post manufacturing powder clearing. An attempt to retain a cross-section around 1.5mm was made to ensure the ease of powder

removal. Wall temperature should not ever exceed a maximum value of the thermal operating limit of Aheadd® CP1 20/63, ~650K. [4]

Cooling strategies were converged upon through a series of thermal and mechanical stress simulations. Rocket Propulsion Analysis (RPA) was used to implement the Bartz equation for heat transfer coefficient through the chamber and nozzle boundary layer. Hot wall temperatures were then inserted into a thermal hoop stress calculation to derive stress values which fed redesign of thermal solutions until a final solution was converged upon. Additionally, a 15% film cooling solution was added to further reduce the thermals reached by the engine and a 1% addition of the additive PDMS will further reduce temperatures at hotspots. This percentage was chosen since, as seen in the graph below, minimal gains are seen past 1%.

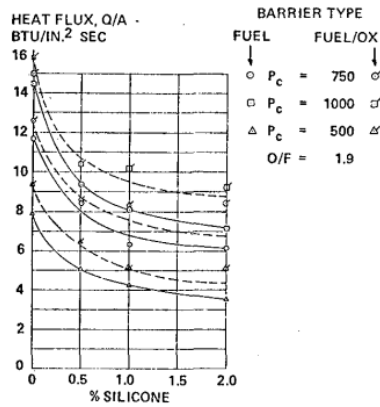


Fig. 12 Throat Section Heat Transfer

Figure 7, Heat flux reduction as a function of PDMS addition

PDMS reduces the total heat flux across the entire engine by creating silicon dioxide upon combustion which is deposited along the engines inner walls and acts as an ablative thermal coating. At 1% PDMS, the expected heat flux reductions are within the range of 25-60% with negligible effects on the performance of the engine [1], [2]. The PDMS additive has been modelled in the thermal analysis of the combustion chamber as approximately a 20% reduction in total heat flux at the throat. This acts as a conservative thermal estimate and does not accurately represent the potential heat flux reductions elsewhere in the engine.

Table 145: Channel Geometry

Property	Value [mm]
Wall thickness	0.8
Rib thickness (Chamber – Throat - Manifold)	0.95 - 0.9 - 1.1
Channel width (Chamber – Throat - Manifold)	5 – 1.5 – 3.5
Channel Height (Chamber – Throat - Manifold)	1.5 – 1.5 - 1.5

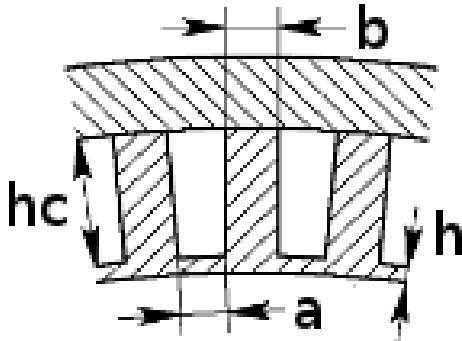


Figure 126: Channel Geometry (figure taken from RPA)

## Thermal simulation results

Table 157: Results of thermal simulations

Property	Value
Maximum chamber-side wall temperature	577 K
Maximum coolant-side wall temperature	569 K
Maximum velocity of coolant	5.74 m/s
Minimum velocity of coolant	1.79 m/s
Maximum heat flux	3844 kW/m <sup>2</sup>
Increase in coolant temperature	73K

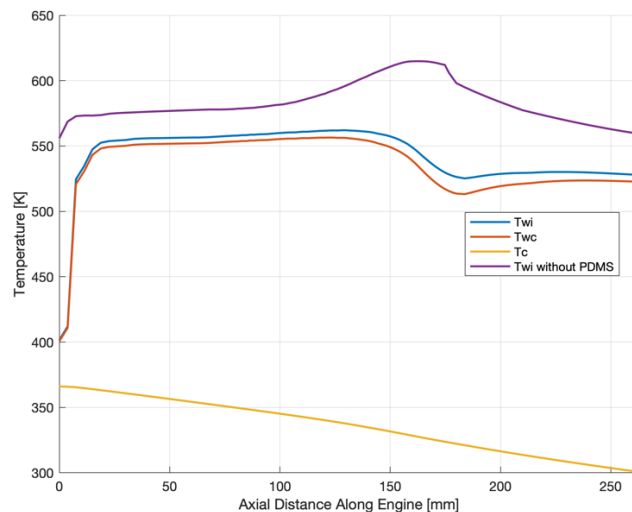


Figure 8, Results from thermal simulations

The graph and table above display the results of the thermal simulations. Twi is the inner wall temperature chamber and Twc is the inner wall temperature of the cooling channels. Tc is the temperature of the coolant and Twi without PDMS is the results of the simulations without factoring in the 20% heat flux reduction at the throat from the PDMS. Even without factoring in the PDMS, the temperatures are still below 650K limit.

## 3.2 Injector Plate

Two injector plate designs are to be machined. Both injectors adhere to the same chamber interface dimensions, this is to allow for interchangeable injector and combustion chamber combinations.

The first of these is an aluminium version of last cycle's like-like impinging design (see Fig), this is to provide a lighter flight version of the existing chamber and injector plate assembly. All geometric dimensions are to be kept the same, so as not to unexpectedly introduce any combustion instabilities.

For the second, a coaxial swirl injector plate is being designed. This plate must be machinable, and the design must feature no inter-propellant seals. This is due to their difficulty to implement and associated risk (NASA, 1976). The injector plate consists of a “double decker” manifold, according to the inlet positions of coaxial swirler elements (see Figure 9).

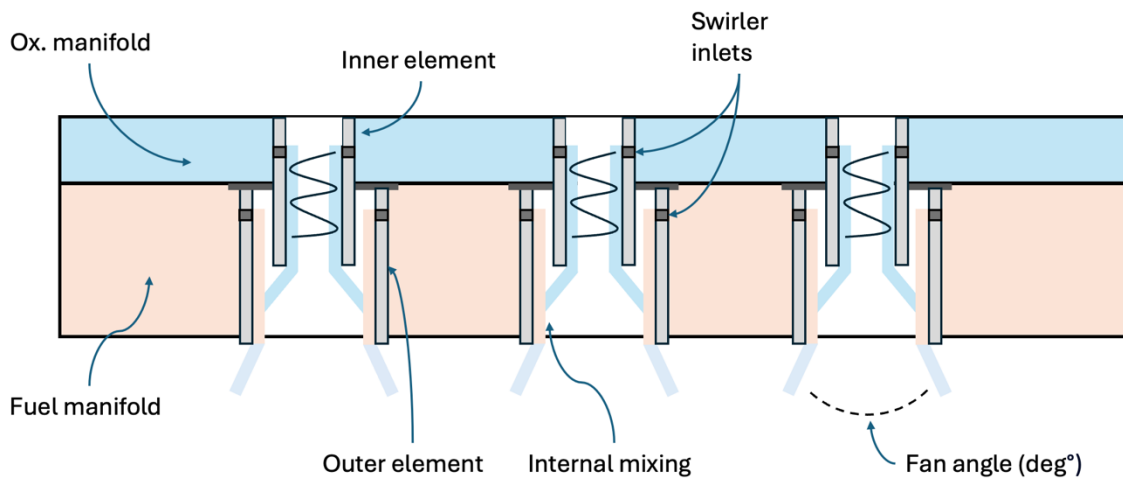


Figure 9 - "Double decker" coaxial swirl manifold principle

The greater the quantity of coaxial swirlers, the better the propellant atomisation and mixing (Bayvel, 2019). Accordingly, the design constitutes five elements to give an optimal balance between the difference in nozzle diameters and number of elements (see Figure 910).

For a given fan angle, the nozzle diameter is proportional to mass flow (Bazarov, 2004). Therefore, for external mixing, the propellant with the greater mass flow must occupy the outer swirler element. To avoid this, an internal mixing design for the swirler elements was chosen (see Figure 10: 11). This allows the fuel from the chamber cooling channels to pass directly into the lower decker manifold, easing the fuel flow and film cooling elements design.

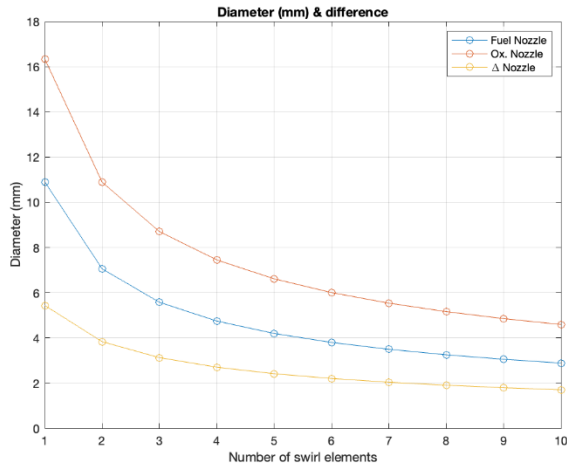


Figure 910: Effect of swirl element quantity to nozzle diameters

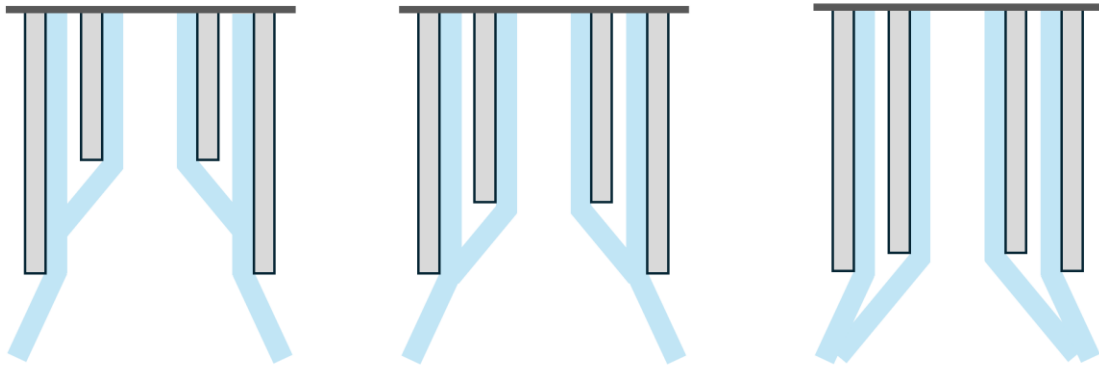


Figure 10: 11 Internal (left), tip (middle) and external (right) mixing types

The central injector section is to be machined from either side of a single piece of aluminium, meaning the middle deck and coaxial swirl element are machined as a single piece. This avoids any direct inter-propellant seals, featuring two propellant-to-atmosphere seals instead.

The swirl element has been sized and cross-validated by the design procedures for closed type swirlers from (Bazarov, 2004) and (Bayvel, 2019). However, machining the swirl element directly with the central plate limits the outer element to an open-type swirler (see Fig). Experimental tests on various coaxial swirler configurations are to be carried out. This is to further validate the cited design methodologies, and to investigate some the effect of this open-type constraint.

### 3.3 Feed System

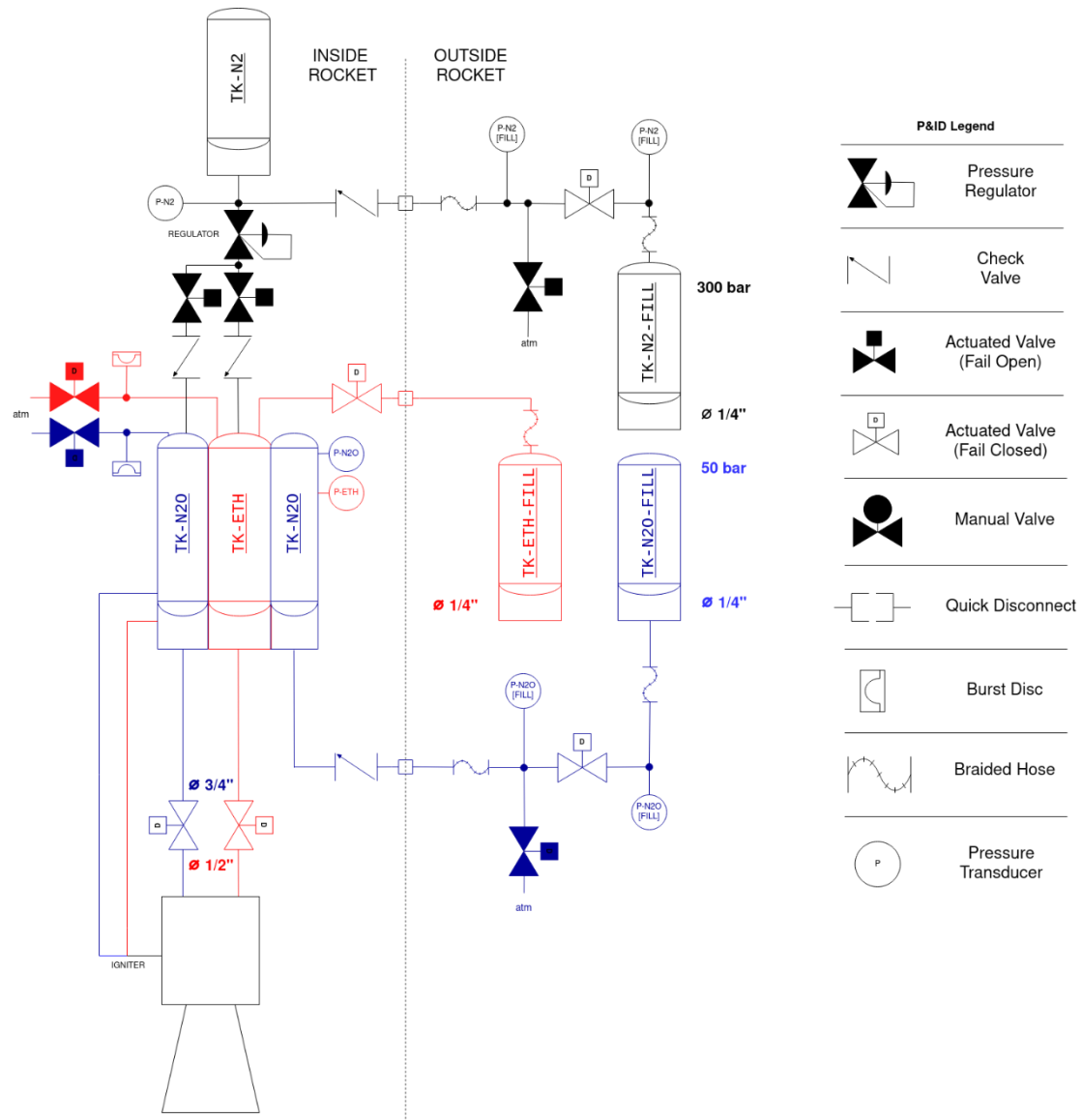


Figure 12 Full System Plumbing and Instrumentation Diagram

The purpose of the feed system is simply to provide to the injector plate a steady supply of high pressure fuel and oxidiser.

The chosen solution is a pressure fed system, with a pressure source of nitrogen. This P&ID shows the plumbing and fluidic components present in the LV and GS. An analysis of last year's integrated hotfire data showed that the system would have worked the flight case (given that all the valves open).

Thus this year we are focussing on iterating and refining, with the addition of an internal igniter, pumped ethanol for faster fuelling, and a general neatening up (with more compact geometry and better lines). Note that there are currently 3 cases for the launch vehicle that are being concurrently developed until March/April.

**Case 1:** Open loop control with mechanical regulator (like last year).

- Proven system from last year, but suffers from droop (steady state error).

**Case 2:** Closed loop control with actuated run valves.

- Potential to allow fine throttling and OF ratio control, but may produce instabilities in flow.

**Case 3:** Closed loop control with electronic pressure regulator (Jake's RP3).

- As above, but without instabilities, but requires fine control at high pressures.

### 3.3.2 Servo-valves

The system currently requires 11 valves to control the fuelling and firing procedures.

COTS actuated valves do not meet our requirements for cost or size, hence a significant amount of design effort is being placed this year on developing a custom solution, with 2 main approaches.

#### *Linkage Design*

A three-bar linkage approach was tested to actuate servo valves, with each bar with 1 Degree of Freedom. This would eliminate the challenges related to misalignment, which commonly occurred last year.

During analysis, about 70% of the stall torque of servo and the breakaway torque of the valve to be higher with pressurised fluid flow was considered. This resulted in at least 1:4.2 to actuate them and linkages were designed accordingly. From simulations bespoke parts needed to be manufactured to ensure to maintain this ratio.

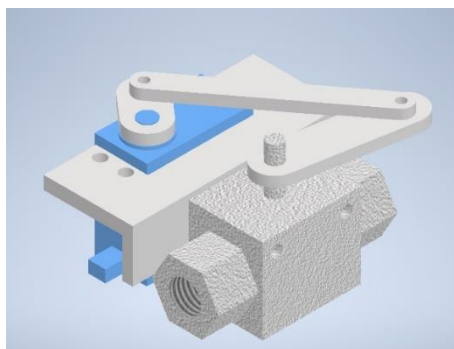


Figure 13 Linkage actuator

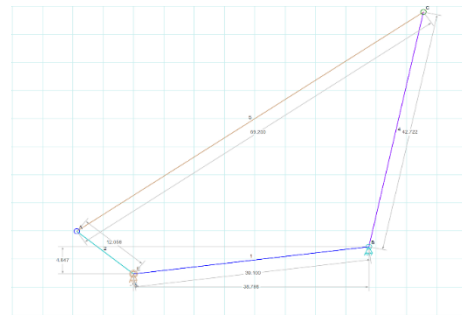


Figure 14 Linkage software simulation

The test was initially conducted on 1/4" one-piece valve, due to a lower breakaway torque. Rapid prototyping is underway using 3D printed PLA, but metal parts will be used in the final design. Testing is currently underway, following which the performance will be contrasted with other designs. Initial testing illustrated an uneven stress distribution, the linkages suffered shearing leading to failure.

From analysis and testing, the major challenges were excessive space usage and actuating valves a full 90° rotation. This can be addressed through more systematic testing with different linkage lengths, for which pin-slot joints (refer Figure 9) are aimed to be machined providing ease in adjusting lengths. Further testing is aimed at mitigating the existing challenges alongside minimising input torque and testing valves at different angles.

#### *Geared Design*

A 1/4" geared servo-valve has been designed and is to be machined from stock aluminium (see Figure 15). A 1/4" COTS Delta-P valve was chosen. This is due to its easy to interface with design, and budgetary constraints. The design features a double ended rod ball bearing tie to ensure tooth engagement. This is a result of previous issues with gear alignment due to the slop (or

“wobble”) in the valve’s head socket. A gear ratio of 1.7 was chosen as a balance between servo gear size, servo range of motion and overall mechanical advantage. A drawback of the chosen COTS ball valves is that of overheating the servo motors through an innate “springiness” in the valve socket. Options of using different valve types and analysis into the servo overheating conditions are being investigated. A current solution is that of back driving the servo a couple of degrees from its set position. This releases the “spring” tension, and as such has been named a “software issue”.

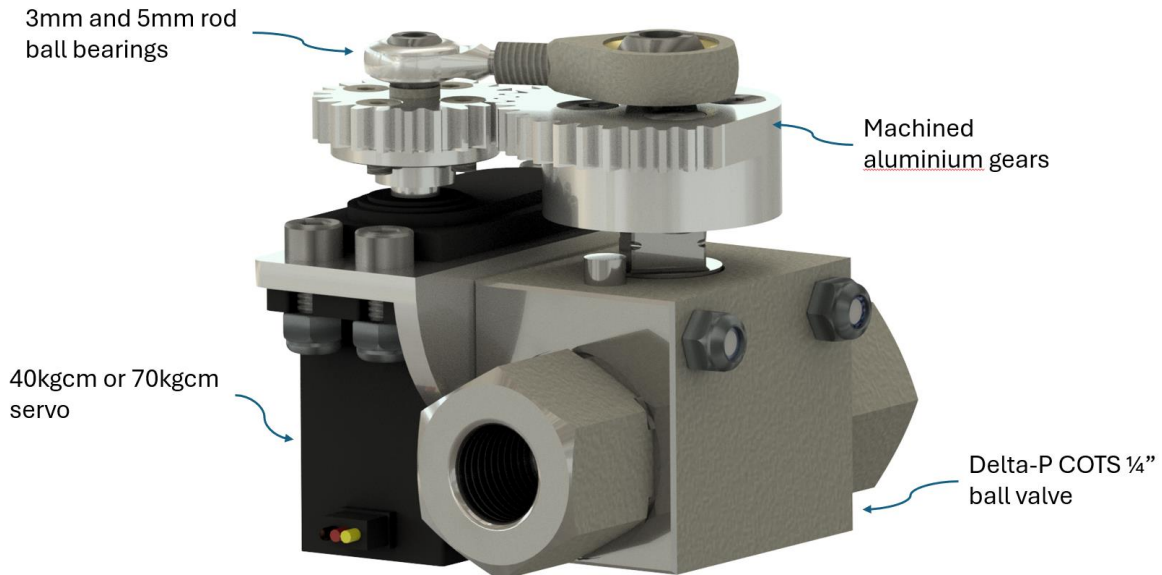


*Figure 15 — 1/4" geared servo-valve*

Likewise, geared  $\frac{3}{4}$ " and  $\frac{1}{2}$ " main engine valves have been designed (currently only head CAD exists). These utilise COTS 3-piece valves. The design consists of two machined aluminium arms attached on the exterior top bolts of the 3-piece valves. This allows for both in-situ mounting, and ease of overall plumbing assembly. The design features a potentiometer aligned with the valve head axis and mounted via a bracket. Full system torque analysis is being carried out, with a pressurised test rig being designed.

Currently, all existing valves utilise 40kgcm  $180^\circ$  servos. These are to be upgraded to 70kgcm  $180^\circ$  servo motors for the  $\frac{1}{4}$ " servo-valve system. This is to provide greater torque overhead. The  $\frac{3}{4}$ " and  $\frac{1}{2}$ " main engine valves feature 70kgcm  $360^\circ$  servos. Servos of this type are controlled through rotational speed and direction. This allows for more precise valve angular control and a timed startup sequence.

### 3.3.3 Computational Model

Lessons learned and data collected on the behaviour of the feed system has allowed us to begin developing advanced computational models of the fluid behaviour. The aim of this is to allow us to tighten margins on tank volumes and pressurisation systems for this and future years, and support development of new methods of control.

### *Characterisation of Nitrous Oxide*

Nitrous Oxide, our oxidiser, is a troublesome fluid. At the temperatures, and pressures we work at (i.e. near the triple point), the substance exists in an equilibrium between its solid and liquid phases.

Since only the liquid phase can flow to the injector, it is important to model and understand the bi-phase behaviour.

This was done through a program of an equilibrium model for a self-pressuring propellant tank (Zimmerman, 2013), with the CoolProp library being used for calculating the nitrous oxide properties at both liquid and vapour phases when in a saturated state. We aim to further develop this to calculate the transient state of the tank as well as to determine the optimal tank volume and mass for a given mass flow rate and drain time from the rest of the rocket. Additional work is also underway for the simpler case of ethanol tank drain and nitrous oxide tank drain due to the flow of nitrogen rather than due to self-pressurisation.

### *Results from the CoolProp model*

For a given tank pressure of 550kPa, tank volume of  $0.0581\text{m}^2$  in an ambient temperature of 298K, the current model predicts the nitrous oxide tank would have a mass of 11kg for a given vapour quality of 0.3. The convention for vapour quality used is that a value of 0 represents saturated liquid and a value of 1 represents saturated vapour.

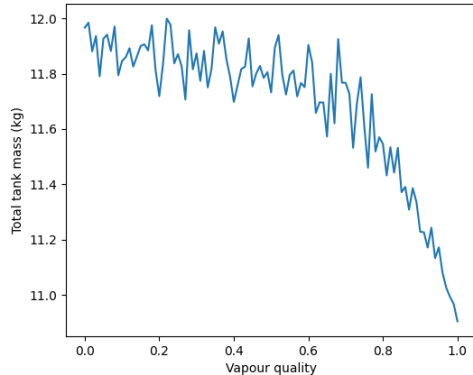


Figure 16 Total nitrous oxide tank wet mass for a given vapour quality.

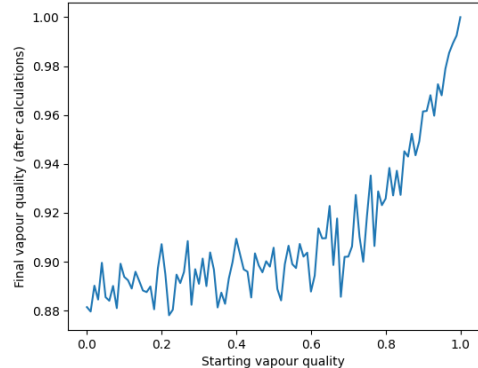


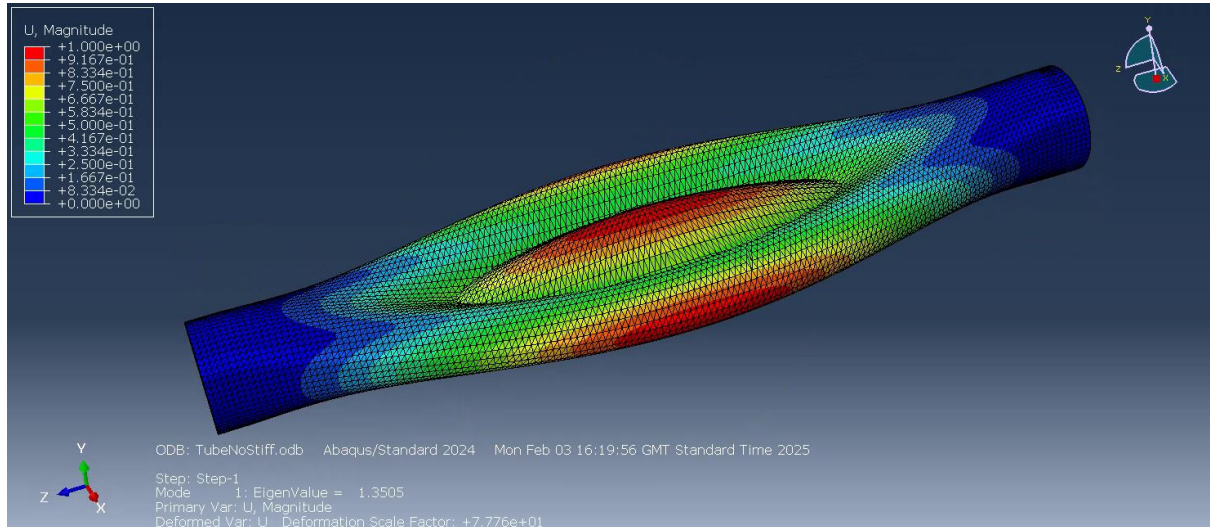
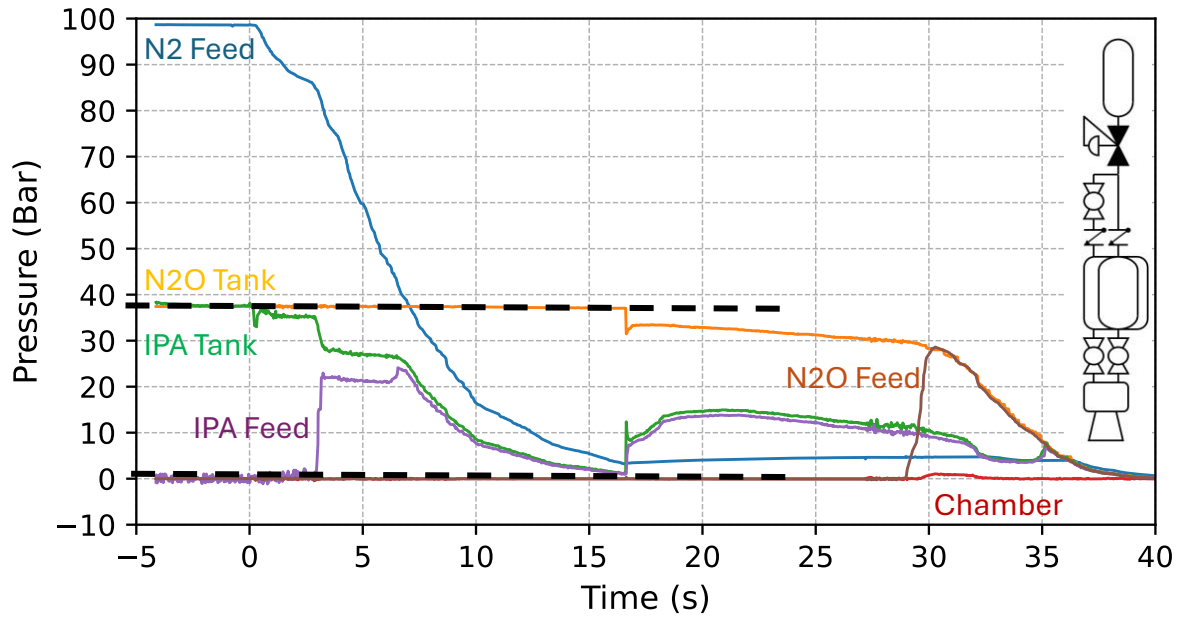
Figure 17 Vapour quality of the nitrous tank during drain.

## 3.4 Coaxial Propellant Tank

### III.4.1 Finite Element Correlation

Previous testing saw a failure in the propellant tank as a result of a ignition failure that lead to a valve actuation failure and ultimately a tank failure. Focus lies on the tank failure as it is the only part of the system which could not be easily and quickly fixed. Ultimately the tank failure led to the end of the testing campaign. An attempt to mitigate this failure going forwards must be supported by full

appreciation and analysis of the observed failure conditions. To this end a revaluation of the simulations of the failure was conducted. We observed in practice a outer tank pressure of 38 Bar acting on an empty inner tank. This pressure gradient is thus the value in which failure occurs. The strategy for simulations was that of simplification. By simply modelling the inner tank with pinned constraints on either end and a force of 30 bar acting in a buckling analysis, a failure pressure of ~40 bar was observed. This is in good correspondence with the observed buckling result.



### III.4.2 Detail design

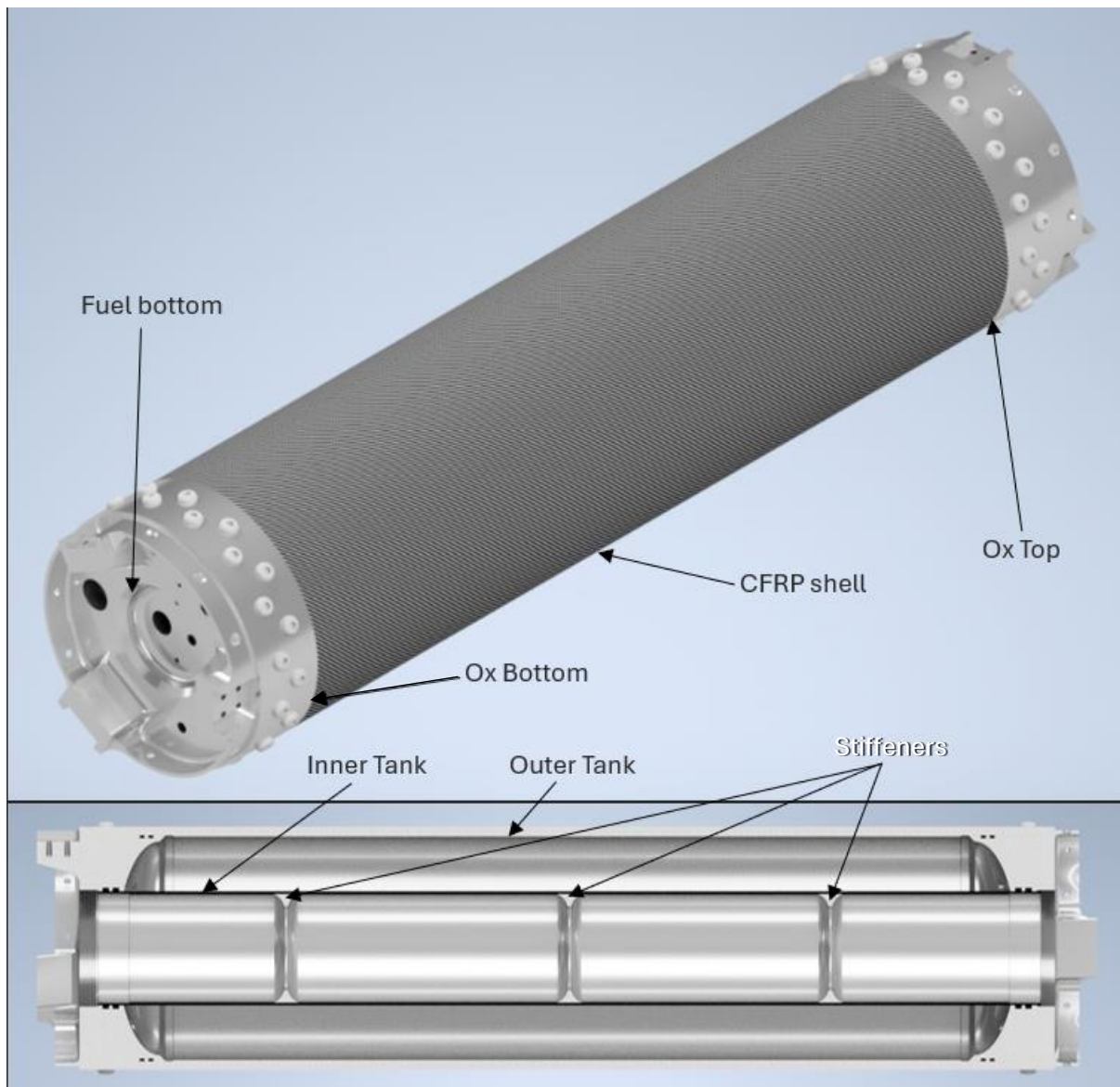
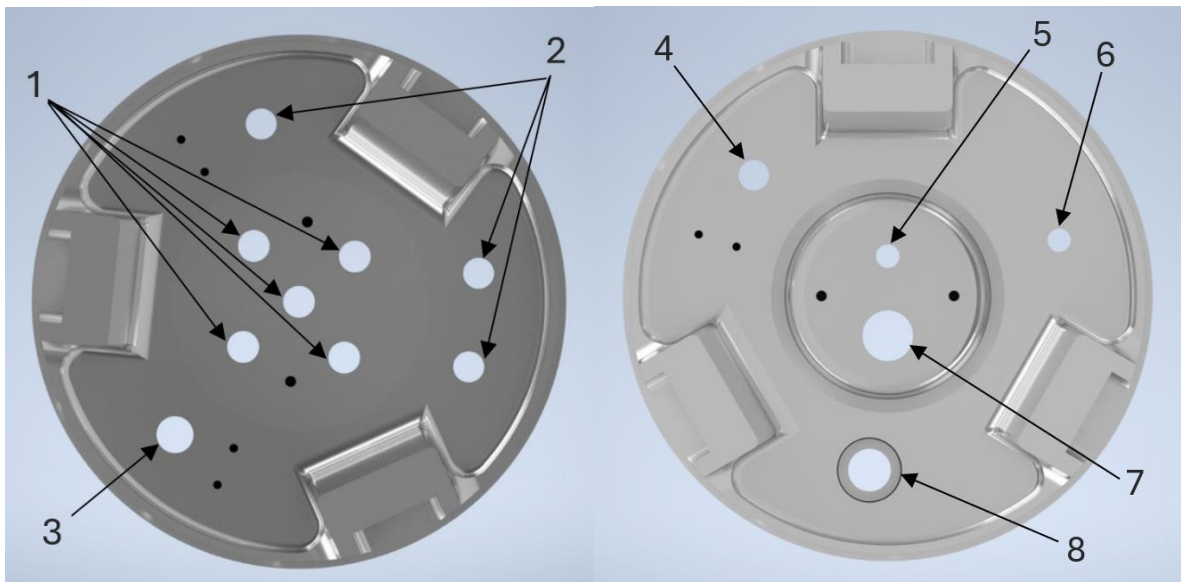
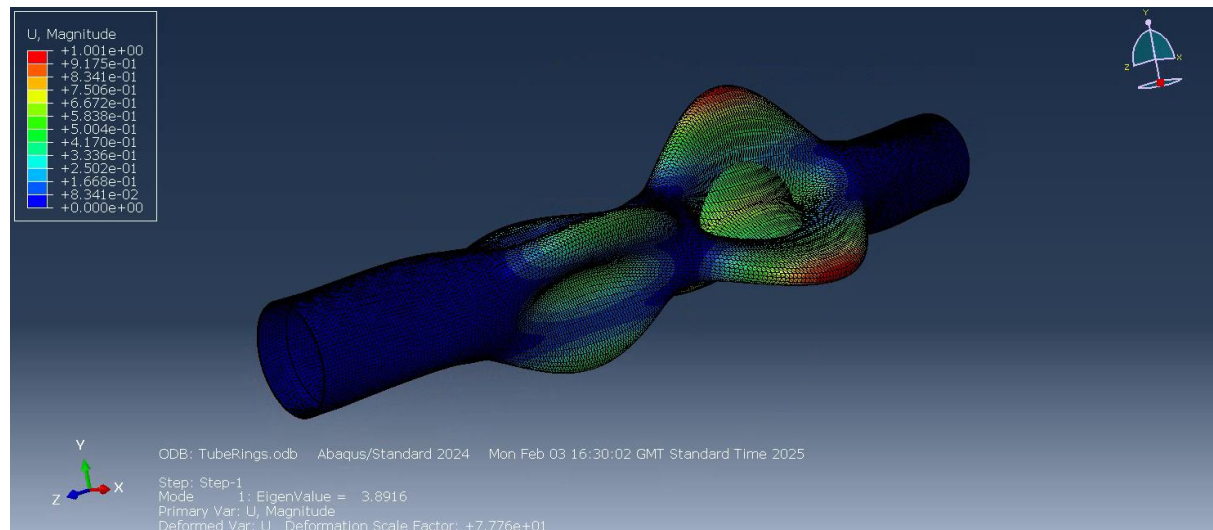


Figure 18 - Half-section view of the full tank assembly

To develop on last years tank, part of the thickness of the outer tank has been removed, and replaced with a CFRP-wrapped shell, which will be done at the NCC. Wrapping the tank will provide crucial weight saving, without risking leakage as the tank is still sealed inside a metal layer. Next steps to implement this involve research on ply orientations, thickness of the sheet, and implementing a CFRP shell to our FEA models.



Label	Port size	Port function
1	5x1/4 BSPP	Pressure in, Fill, Transducer, Vent, Burst Disc
2	3x1/4 BSPP	Pressure In, Transducer
3	1x1/4 NPT	Diptube/Vent
4	1x1/4 BSPP	Fill
5	1x1/8 BSPP	Ignitor
6	1x1/8 BSPP	Ignitor
7	1x1/2 BSPP	Flow out
8	1x3/4 BSPP	Flow out



To solve the issues of buckling encountered when only the oxidiser tank is filled, 3 stiffening rings have been added on the inside of the inner tank. The stiffening ring is shown in Figure X (on left) and was designed with a highly filleted surface in order to ensure smooth fuel flow. Using the same methods as in Figure X (non-stiffened FEA), an eigenvalue of 3.89 was observed, giving a pressure of 116.7 bar, as shown in Figure X (stiffened FEA). This is well within the range of 2xMEOP (100 bar) using the current design.

### III.4.3 Design for Manufacture

The goal was to design parts that are easy and cost effective to produce. Therefore, the Tanks team worked closely with Jack Marsh, technical specialist at the university, who suggested using fillets radius size from 3 mm to 12 mm because these drill heads are readily available at the workshop. Moreover, a clearance gap between two edges that need to be filleted should be twice the radius of the fillet in order to simplify CNC work. Additionally, having sloping edges greatly increases job time and leads to a poorer surface finish. Hence, keeping this new information in mind, the team discovered two ways that the design can be optimised for machining.

#### a) Weight saving cut outs on the Ox-Top/Bottom

Last year's final iteration of this part had complex weight saving cut-outs that had bottom edges filleted throughout without keeping a clearance gap between the two edges. To simplify machining the parts, the team decided to scrap the cut-outs altogether.

After gaining some clarity by the insights given by Jack, cut out shapes like triangles and trapeziums, instead of last year's curved complex shapes, mitigated the clearance gap issues. This will be updated for our new design.

#### b) Stiffener

The current stiffener has a fillet radius of 14 mm, which will be changed to 12 mm. Moreover, as you go toward the symmetry line, after the filleted part, the lip needs to be flattened out.

When looking at the tank as a whole, there are two assembly problems that the team found out

#### a) Sliding the three stiffeners through the Inner Tank at accurate distances

Metal glue will be used on the cylindrical surface of the stiffeners to bond it to the inner tube. There were two proposed solutions to assemble the stiffeners. First, inserting a cylindrical foam through the stiffeners and then pushing the foam down the inner tube, then melting the foam using acetone. Second, using a cam lock system to use a shaft to push the stiffeners down the inner tube then unlocking it and pulling it out. This method requires creating holes and gaps in the stiffeners.

#### b) Wrapping CFRP over the Outer Tank

After machining the outer tube, it will be taken to the National Composites Centre to use their film winding machine to wrap the outer tank with Carbon Fibre.

### III.4.4 Testing Plan

Hydrostatic testing to pressure as defined in DTEG

Type of Testing	Description	Duration (mins)	Test site requirements
Hydrostatic test (Tests will be done on the inner tube with o rings and outer tube separately at 82.5 bar and done together.)	1. Increase pressure to 82.5 bar in 10 bar increments, holding at each interval of 10 bar 30s.  2. Watch pressure gauge for leaks over 30 minutes.	120	¾ inch high pressure water BSPP fitting or adapter. Containment area. Remote pressurisation Drainage.

	3. Relieve pressure in system. 4. Inspect system for any damage.		

## 10 Pages for Propulsion

## 4. Launch Vehicle

### 4.1 Aerostructure

#### Introduction and design philosophy

The structural design builds on last year's iteration with refinements for mass reduction, improved subsystem integration, and robustness. A test-informed approach using experimental results and FEA guides decisions. Key structural components include Composite Structures (CFRP nosecone, panels, fins; GFRP payload tube) and Isotropic Structures (Aluminium 6082-T6 frame (stringers, bulkheads), composite-metal coupler, fin-can coupler, airbrakes).

Load cases analysed include launch loads, max dynamic pressure, burnout, parachute deployment, and impact. FE simulations focus on static and buckling analysis due to axial compression and interfaces (“4.2kN axial engine” and “275N above tank lift”). All analyses use Abaqus CAE with a safety factor of 1.5–3.

#### Nosecone

The existing nosecone, made of 600gsm CFRP in an epoxy matrix with a [-45/0/45] lay-up and an aluminium tip, will be reused after further analysis for improved aerodynamic performance. The nosecone follows a Von Kármán profile with a 200mm outer diameter and a total length of 770mm. Improvements have been identified, including a misalignment at the aluminium tip joint, an excessive safety factor, and surface finish quality contributing to aerodynamic inefficiencies. The maximum stress of 0.667MPa and a buckling load of 6340kN resulted in an excessive buckling safety factor, suggesting a redesigned lighter nosecone could be manufactured for better rocket efficiency if times allows. A single modification is planned to address joint misalignment, trimming the composite section and fabricating an extended aluminium tip.

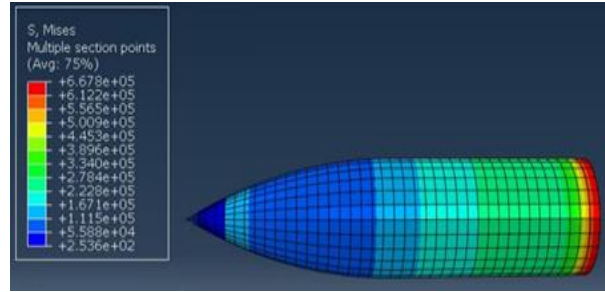


Figure 20: FEA of nosecone (Von Misses stress results)

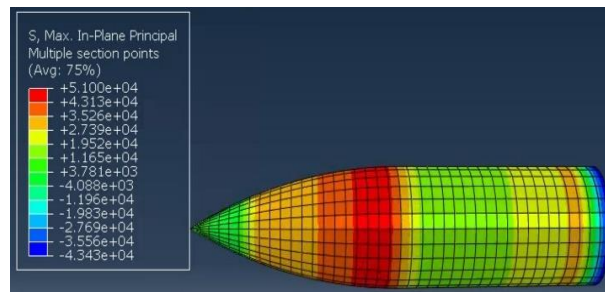


Figure 19: FEA of nosecone (Principal stress results)

#### Payload Tube

The payload tube design aims to reduce mass while maintaining structural integrity. The tube is made of a glass fibre-reinforced polymer composite with an epoxy matrix and a woven E-glass fabric. The previous tube had manufacturing defects due to excessive resin content, fabric displacement, and resin-starved regions. The redesigned tube retains its geometry but undergoes lay-up optimization via FEA and improved manufacturing control. Team members trained in wet lay-up techniques ensure proper fibre alignment, optimized resin distribution, and minimized fabrication defects. A three-step approach was designed to evaluate the impact of fabrication inconsistencies: FEA analysis of an Ideal Tube (compression and shear simulations predicted a maximum stress of 2.48 MPa and a buckling load of

148 kN), Non-Destructive Testing (NDT) testing, and a compression test of a cut section. Correlating computational, NDT, and experimental data will refine quality control measures, leading to a more reliable, lightweight, and structurally optimized payload tube. Lessons learned will inform future composite fabrication improvements.

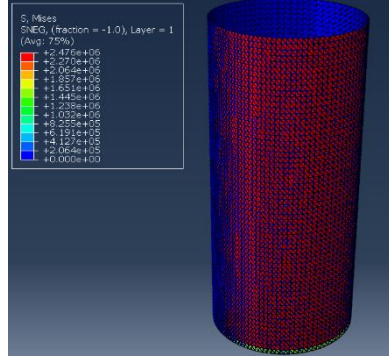


Figure 21: FEA of Payload Tube (Von Mises stress results)

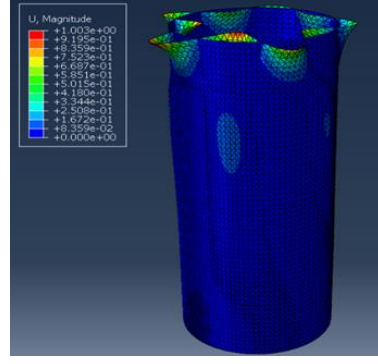


Figure 22: FEA of Payload Tube (Linear Buckling First Mode results)

## Fins

The fins must be designed to be aerodynamically efficient and strong, with a carbon fibre outer structure bonded to a core material. The design includes an asymmetric [+45/-45/0] layup to improve torsional and bending resistance. The fin canisters will be made using advanced manufacturing techniques like Prepreg Carbon Fibre or Injection Moulding. Two designs are under review: a one-piece design, which is stronger but more complex, and a clamshell design, which is more accessible but requires reinforced bonding. A robust attachment system will be implemented to prevent failure under dynamic loads. Fillet integration methods, including co-moulding, external carbon fibre reinforcement, and bonded pre-manufactured fillets, are also being considered to reduce stress concentrations.

## Metallic Frame (Stringers & Bulkheads)

The rocket's primary load-bearing structure consists of a metallic frame, including the thrust structure, coaxial tank, and feed system support structure. A Functional Efficient Analysis (FEA) was conducted on the feed system support structure to optimize mass while maintaining structural integrity. A similar approach will be applied to other frame components, incorporating more precise load cases. The feed system support structure consists of two bulkheads connected by three stringers, which carry most of the loads and serve as mounting points for other subsystems. The large unsupported stringer section raised concerns about buckling, prompting an analysis to determine if mass reduction was feasible. FEA on the existing stringer design yielded a maximum Von Mises stress of 3.058 kPa, well below the material's yield strength (255 MPa). A new design was proposed, reducing stringer thickness and flange length, decreasing mass from 0.838 kg to 0.464 kg per stringer. Manufacturing constraints prevent further reductions in thickness below 2.5mm due to machining limitations. FEA on the

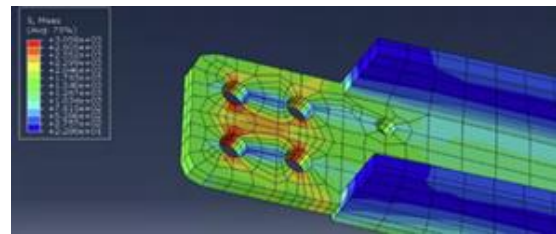


Figure 24: FEA of previous year's stringer (Von Mises stress concentration around bolt holes)

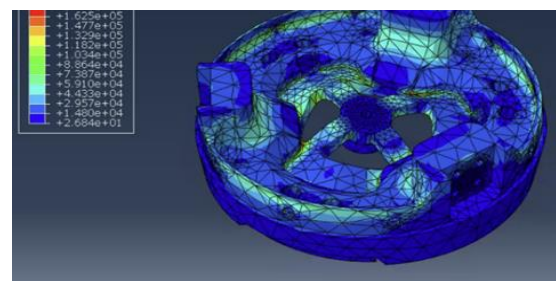


Figure 23: FEA of bulkhead (Von Mises stress results)

bulkheads resulted in a maximum Von Mises stress of 0.1773 MPa and a buckling load of  $1.33 \times 10^9$  N, with a safety factor of 728. Further optimization will involve modelling stringers and bulkheads as an integrated structure with refined load cases.

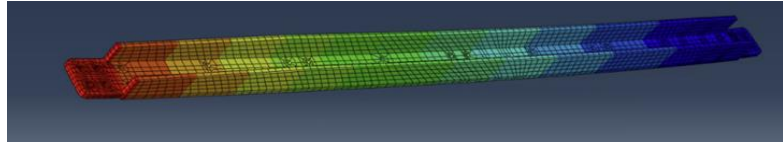


Figure 25: FEA of previous year's stringer (Linear Buckling results)

## Nosecone Coupler

A metal coupler has been introduced to improve the structural integrity of the composite nose cone and fuselage. This component is designed to withstand higher loads, reduce stress on composite edges, improve load distribution, and ensure a seamless connection. Initial design iterations included a coupler with an outer diameter of 20mm and an inner diameter of 19mm. The third design refined the connection by repositioning the face fillet and incorporating 2mm holes for shear pins. FEEA simulated a 275N load and found negative eigenvalues in buckling analysis, requiring thickness and height adjustments to prevent structural failure. Further optimization will determine the ideal dimensions for weight reduction without compromising integrity.

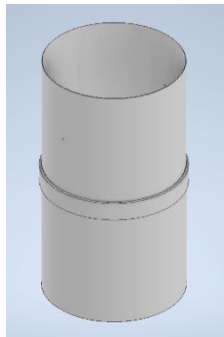


Figure 26: Third coupler design

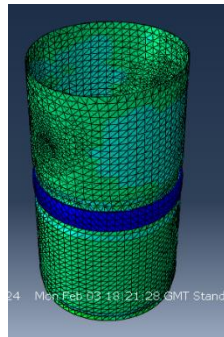


Figure 27: FEA of coupler design (Von Mises stress results)

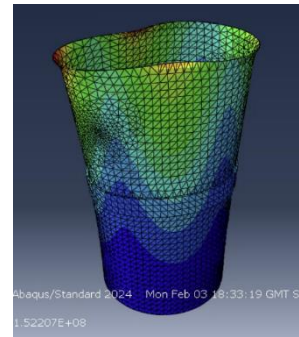


Figure 28: FEA of coupler design (Linear Buckling results)

## Fin-Can Coupler

To accommodate vertical airbrakes, the fin-can must have a larger diameter than the fuselage, requiring a coupler to minimize drag. Manufacturing the fuselage, fin-can, and coupler as a single composite piece is impractical due to tolerance constraints. A separate composite tubing option was considered but would negate the benefits of a metal coupler. Consequently, a metal coupler between the fuselage and fin-can is the most viable solution.

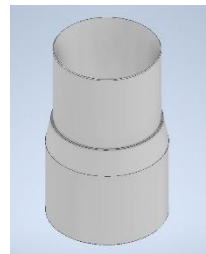


Figure 29: Fin-can coupler metal design

## Airbrakes

Last year's airbrake system used a gear-driven mechanism to deploy petal-style airbrakes, increasing drag to limit apogee. While mechanically simple, several issues were identified: Fin Misalignment - Gear ratios were inaccurate, preventing full retraction and causing uneven drag; Suboptimal Retraction - Fins did not sit flush, inducing unwanted drag and flow effects; Mechanical Play - Gear mechanism exhibited significant play, leading to inconsistencies in deployment; Limited Drag Area - The estimated

required drag surface was 17,500 mm<sup>2</sup>; Sharp Edges on Deployed Surfaces - Potential interference with parachute deployment and safety concerns.

A triple push-rod mechanism was considered to address fin alignment, reduce mechanical play, and allow fins to sit flush. Additionally, stacking multiple units could increase drag but at the cost of added weight and complexity. This solution would, however, increase the weight and mechanical complexity of the system.

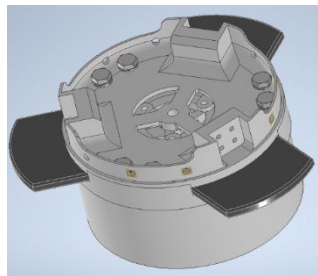


Figure 31: New airbrake mechanism (general integrated view)

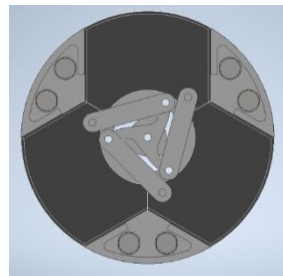


Figure 30: Stored internal airbrake mechanism (top view)

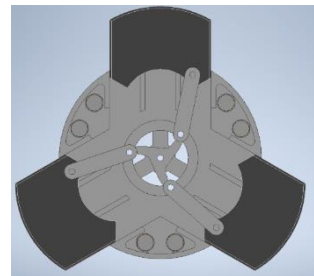


Figure 32: Deployed internal airbrake mechanism (top view)

A vertically deploying airbrake system was also evaluated, offering increased drag area by utilizing panels that deploy perpendicular to the fuselage. However, this design introduces significant moments on the hinges, potentially causing actuation difficulties and flutter.

## Panels

The panels serve as both aerodynamic closure surfaces and structural supports, bolted to metallic stringers that form the primary frame. While not the main load-bearing component, they must withstand aerodynamic loads and extreme failure scenarios. This year's design reduces panel mass while maintaining structural integrity, improving on last year's [45/0/-45] CFRP and [0/90] GFRP plies. Last year's 3D-printed surface adaptors for bolting to stringers may be replaced with metal components for better load transfer, and a lip extension is being considered to prevent fluttering on the upper edges during ascent. Structural optimization efforts include mass reduction and refined hole distribution via FEA-driven analysis, with improved bolt interaction modelling using coupling constraints and reference points. Initial shear simulations up to 4.2 kN are in progress, with planned buckling, bending, and vibration tests to ensure elastic stability and guide further weight-saving strategies.

## Further work

Further work will refine structural design through advanced simulations, including detailed FEA for buckling, bending, and torsion, as well as getting more accurate load prediction using CFD and wind tunnel testing for aerodynamic performance. Experimental validation will involve NDT for defect detection, flutter testing in wind tunnels, compression and tensile testing for simulation validation and prototype manufacturing of mechanisms. Manufacturing improvements will focus on optimizing composite lay-up, enhancing resin distribution, and reducing defects.

## 4.2 Aerodynamics

### 4.2.1 Aerodynamic Design

#### 4.2.1.1 Nose cone design

The nose cone design has stayed the same as last year's because the Von Karman shape is optimum for minimum drag at high speeds. A MATLAB script was used to get the points in a CSV file for the shape of the nose cone. The MATLAB script provides precise information about the length, radius and number of points of the Von Karman shape. It plots these points on an x-y plane which were then inputted into Inventor to get a rough shape that was joined with the interpolation spline as shown in the image below.

The design minimises the boundary layer separation which improves the stability. By optimising the curvature and taper of the nose cone, the design reduces the pressure drag and allows for a smoother transition of airflow after the pointed tip. This results in a more uniform pressure distribution along the surface. The difference between the Von Karman and an elliptical nose cone that allow it to be better is that the Von Karman produces weaker shockwaves due to a more gradual curvature after a pointed tip.

The Von Karman shape is part of the Haack Series which is a continuous set of shapes determined by the value of C, a variable that defines the nose cone shape. Two relevant values of C are C=0 and C=1/3. When C=0, the LD signifies minimum drag for a given length and diameter and when C=1/3, the LV indicates the minimum drag for a given length and volume. The LD Haack is the synonymous to the Von Karman nose cone (shown below).

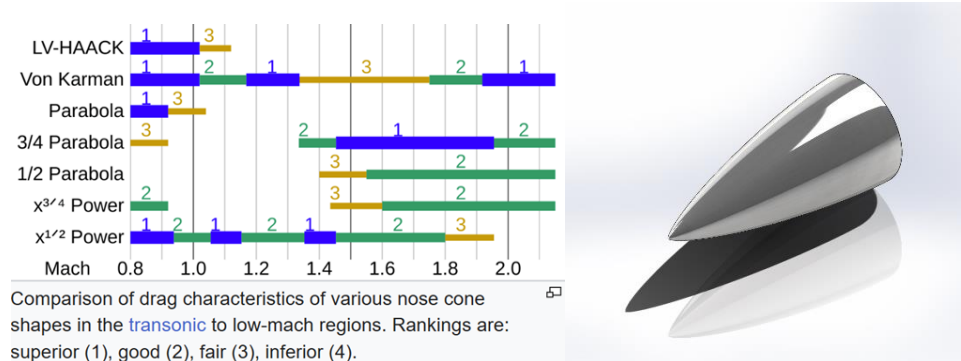


Figure 33: Nosecone drag characteristics

The plot compares the most relevant nose cone shapes. As we aim to go at higher speeds, the only two suitable shapes are the Von Karman from the Haack Series which has some weaknesses from Mach 1.3–1.7 and  $X^{(1/2)}$  from the Power Series which fluctuates with its drag characteristics. The discrepancies in the Von Karman from Mach 1.3 – 1.7 could be due to the increased strength of the shock waves at transonic speeds that cause intense wave drag. Overall, the Von Karman nose cone remains the optimal choice for minim

ising the drag at high speeds due to its ability to reduce the pressure drag and boundary layer separation. Compared to the other nose cone shapes, particularly the Haack and Power series, the Von Karman provides a well-balanced aerodynamic solution for achieving stability and efficiency.

#### 4.2.1.2 Airbrake design

Previously, our primary focus for the rocket's air-brake system was ensuring mechanical reliability and structural robustness against flight loads. However, we have now emphasized the critical aerodynamic aspects—particularly ensuring stability is maintained throughout the operational envelope of speeds and deployment angles while generating sufficient drag to lower apogee by the distance needed. In designing these petal-style air brakes, we are refining their shape and carefully selecting thickness to balance strength, weight, and resistance to flutter, especially near transonic speeds. To further boost drag, we are evaluating a deployment mechanism that enables the petals to extend significantly beyond the rocket's outer mold line, potentially stacking them on top of each other for maximum exposed surface area. Because the rocket is over 4m tall, this stacking approach should have minimal impact on overall stability. While this configuration increases drag, it also adds mechanical complexity, weight, and potential aerodynamic interference between petals.

To refine the boundary layer thickness estimate, we use the second occurrence of Mach 0.3 as the reference speed for air brake deployment, based on flight simulations from last year's TR. Using the density at this altitude, the Reynolds number at 1m, 2m, and 3m down the rocket is recalculated. The boundary layer thickness at these positions is larger than initial estimates, requiring air brakes to protrude beyond 16.7mm at 1m, 29.9mm at 2m, and 40.8mm at 3m to engage with undisturbed, high-energy airflow, maximizing their effectiveness. The flow remains turbulent until approximately [transition speed TBD], at which point this calculation method is no longer valid. However, we primarily focus on Mach 0.3 for stopping potential, as at much lower speeds (e.g., Mach 0.01), aerodynamic braking is ineffective due to insufficient airflow interaction.

Additionally, given that the final location of the air brakes is still being optimized, we recognize that positioning them further rearward could enhance overall stability. However, this comes at the cost of reduced drag efficiency due to the thicker boundary layer in this region. Finally, while we are evaluating the removal of the drogue chute, this will not impact the total descent speed or drift distance but would eliminate the requirement for a dual deployment recovery system, simplifying operations. By optimizing thickness, reinforcing hinge points, refining the overlapping geometry, and validating our deployment conditions through CFD and past flight data, we aim to develop a reliable, flutter-resistant air brake system that effectively decelerates the rocket without compromising stability.

#### 4.2.1.3 Fin design

Through research, a double wedge profile with a rounded leading edge was considered most adequate for subsonic flight (seen in Figure X). However, given the large use of symmetric aerofoils for subsonic flight, a combination of a double wedge and a symmetric aerofoil was designed. The previous iteration of the fin comprised of trapezoidal fins that were oversized and conservative. While this design provided a robust performance, there were weight and drag penalties. The trapezoidal shape offered valuable characteristics with excellent aerodynamic efficiency, strong structural integrity, and a straight-forward manufacturing process.

The new fin design initiative focuses on:

- Reducing design conservatism without compromising safety
- Maintaining stability while achieving weight reduction
- Minimizing drag compared to the previous iteration

There are two proposed design options:

##### Option A: Rounded Leading Edge Double Wedge

- Variable thickness profile (6% to 12%)
- Key features:
  - Rounded leading edge optimized for subsonic performance

- Superior shock formation management compared to sharp leading edges
- Sharp trailing edge design for:
  - Base drag reduction
  - Clean flow separation characteristics
  - Minimized wake turbulence

#### Option B: NACA Leading Edge Double Wedge

- Incorporates NACA airfoil benefits with enhanced performance characteristics
- Distinguished features:
  - Refined leading edge profile for improved aerodynamic efficiency
  - Flat outboard edge design providing:
    - Clean, predictable separation lines
    - Organized flow pattern maintenance
    - Reduced tip vortex strength
    - Lower associated drag penalties
  - Optimized outboard section performance

The refined design options maintain the beneficial aspects of the original trapezoidal planform while incorporating advanced aerodynamic features for improved performance. Both options represent a calculated step away from over-conservative design, offering optimized solutions that balance safety with efficiency.

An optimized profile will be obtained through numerical testing providing minimum drag. The fin dimension ensured stability yet was retained too large. This was due to the lack of data obtained on the fin's performance. Hence, the innovative design aims to achieve a good aerodynamic performance, within stability margins, despite having smaller fins. A tapered design was chosen as it is the most efficient in minimizing drag and achieving a robust control over the rocket. Tapered swept was considered shift the Aerodynamic Centre aft but, was disregarded. The use of fairings will reinforce the structural as well as aerodynamic performance of the fins. The final concept design was determined to be the following:

*Table 8: Fin design*

Feature	Measurement	Unit
Root chord	250-300	mm
Tip chord	125-150	mm
Taper ratio	0.5	/
Aspect Ratio	~2.5	/
Semi-span	235	mm

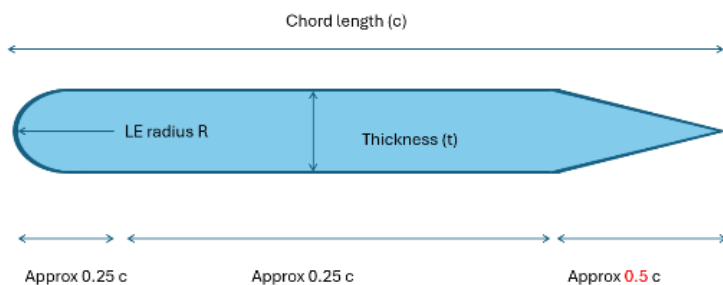


*Figure 34: Fin design*

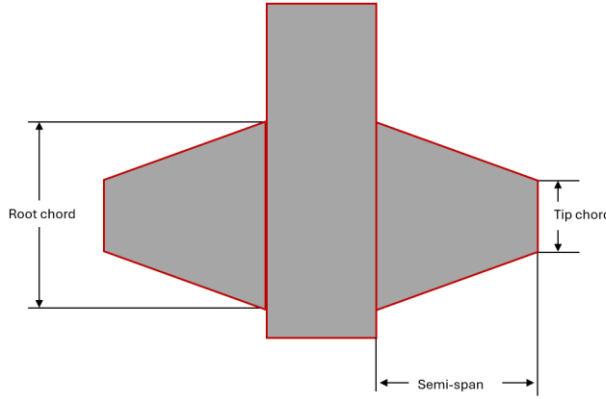


*Figure 35: Fin design*

The fin placement will be determined with respect to the shift in CG during the trajectory.

#### 4.2.2 Numerical Methods for Simulation

No data has been collected in the past using numerical simulation. Hence, the use of software for validation of past and current designs was necessary. In order to predict the aerodynamic behaviours of the rocket and make design choices accordingly, various CFD simulations are being done. However, CFD is complex to set up and run, making it very time consuming. Uncertainties are high with CFD as there is no error control and errors can easily arise from factors such as mesh size and boundary conditions. This makes it not ideal for initial designs. With the use of PanAir (Panel Aerodynamics) certain predictions can be done in a much more efficient and, in some cases, accurate manner.

PanAir is a computer program that uses a high order panel method to solve boundary value problems for subsonic and supersonic potential flows. Panel methods use the Prandtl-Glauert equation (unlike CFD which utilizes Navier Stokes equations) so the flow is assumed to be inviscid, irrotational, linear, and often steady. This prevents the prediction of important flow behaviors, such as transonic shocks, separation and skin friction drag. Yet these complications can be overcome by applying the Kutta condition and combining the panel method with various other methods that can account for the physics neglected by the Prandtl-Glauert equation.

For simple geometries in subsonic and transonic regimes, potential flow theory works quite well. Therefore, for our rocket, PanAir can be just as reliable and far more efficient at predicting aerodynamic elements, including drag, lift and pitching moments, in cases where CFD simulations become highly complex and computationally difficult.

A MATLAB program is being developed to confirm the values obtained for the pressure distribution around a profile and the resultant forces experienced in extreme situations. A simple code which uses subsonic Isentropic relationships to calculate the change in pressure around the profile at different velocities was used.

GridPro is being used to create meshes for the different fin geometries as well as airbrake designs. SU2 is the CFD app utilized to perform accurate simulations in the following conditions:

Different profiles at the average trajectory speed of  $M=0.6$

*Table 9: Airbrake deployment Mach numbers*

Undeployed airbrakes:	Deployed airbrakes:
Mach 0.3	Mach 0.3
Mach 0.6	Mach 0.2
Mach 0.8	Mach 0.1

Testing in the most extreme conditions will gather data on the fins in terms of stability and structural performance. Further, simulating the airbrake deployment will demonstrate the effect of the breaks upstream of the fins during breaking. Despite not being aligned, the airbrakes could have a severe effect on the fins' authority on the rocket. The choice of using a NS solver for a transonic regime is appropriate to simulate any unexpected shocks which might alter the flow. To obtain simpler solutions, an Euler solver will be used. Deploying the airbrake will cause a transition to a turbulent state. Hence, a  $\kappa - \omega$  or  $\kappa - \varepsilon$  solver will be used to simulate the state of turbulence caused by the airbrakes. Performing such simulations will ensure a robust approach to down selecting the final design of the aircraft

#### 4.2.3 Wind Tunnel Testing

##### 4.2.3.1 Introduction to Testing Aims

The wind tunnel model shall be a 50% scale model of the full-sized rocket. Testing shall be performed in the university of Bristol 7 x 5ft wind tunnel, at a velocity of 40 m/s. This is equivalent to a Reynolds number of  $4.72 \times 10^6$ . There are two main drivers behind the need for wind tunnel testing. The first is to gather data which can inform rocket design, for instance, from the characterisation of drag increase upon deployment of the airbrakes. The second driver is for CFD simulation correlation.

The main flight condition we are hoping to simulate is the deployment of airbrakes. With an apogee target of 3000m, the region at which airbrake deployment occurs is 2300m. At this point, the rocket is travelling at a Mach number close to 0.3. These flight conditions result in a Reynolds number of  $1.94 \times 10^7$ , with the reference dimension taken as the length of the rocket. Therefore, the Reynolds number of the tunnel test is around an order of magnitude lower than the true flight case. This is currently unavoidable due to testing limitations; due to test-section area limitations, the 50% scale model is a necessity. Also, the maximum windspeed of the tunnel is 40m/s. These limitations must be considered when assessing any data acquired from the testing. It is essential that proper post-processing is performed on the data acquired for the tunnel flow conditions. With a good understanding of the tunnel flow conditions, enabled by this data, the team may be able to extrapolate conclusions for the true flight condition.

##### 4.2.3.2 Project Timeline

*Table 10: Project Timeline*

Phase	Start	End	Description
<i>1: Planning and preliminary design</i>	20 <sup>th</sup> January	12 <sup>th</sup> February	-Review of previous models and preliminary research into tunnel testing techniques. -Planning and delegation of tasks. Discussion and hand drawing of initial design concepts. -Preliminary CAD and design trade-offs.
<i>2: Detailed wind tunnel model design</i>	12 <sup>th</sup> February	10 <sup>th</sup> March	-Design tasks assigned, detailed CAD design performed. -Review of all progress twice weekly.
<i>3: Manufacture and build</i>	10 <sup>th</sup> March	21 <sup>st</sup> April	-Machining of all metallic parts. 3D-printed parts manufacture. Assembly.
<i>4: Testing systems development</i>	20 <sup>th</sup> March	5 <sup>th</sup> May	-Research and development into tuft tracking system and imagery. -Development of data acquisition method for pressure scanner, methods to store and process data.
<i>5: Wind tunnel testing week 1</i>	2 <sup>nd</sup> June	6 <sup>th</sup> June	-Set-up performed in the first two days, followed by warm-up runs. -Priority : Air brake PID gain tuning
<i>6: Wind tunnel testing week 2</i>	9 <sup>th</sup> June	13 <sup>th</sup> June	-Aero development week : perform sweeps for airbrake deployment, fin alignment, model yaw.

#### 4.2.3.3 Test Plan and Specification

The timeline presented in Table 10 gives proposes 2-weeks of testing, however this is contingent on the quantity of tunnel testing time we are designated. The first two days in the first week of testing will involve the set-up of the model within the tunnel. This will involve ensuring the model is assembled and quality-checked within the tunnel. It will be essential to ensure that any gaps between panels are taped, putty applied to bolt holes, and all components are secure. The team will check that each testing configuration can be achieved, according to the test specification. Also, all testing instrumentation shall be prepared and tested to allow for smooth operations during subsequent testing. Specifically, the acquisition of pressure data shall be performed using the Chell MicroDAQ-3, a 16-channel pressure scanner. With the capability to output differential or absolute pressure data, this scanner can achieve speeds up to 400Hz per channel and transmission of data via Ethernet or a CAN bus. The flow on the surface of the model shall be visualized using tufts, small pieces of nylon thread, the movement of which can help highlight key flow features.

The team shall also gain familiarity with all test controls and procedures. Depending on the rate at which the set-up tasks are completed, initial runs will be performed on the second day. The preliminary runs will be performed in default configuration to provide a datum, a reference point against which any change in configuration may be compared. This testing will also allow for an understanding of the interaction of the wind tunnel strut. For each run, both a wind-off and wind-on run shall be carried out to tare the force balance. The first week of testing should be prioritized towards working with the control and electronics group to tune airbrake PID control gains. The second week shall be focused on gathering data for aerodynamic development. Key aspects of this will be assessing the effect of different airbrake deployments, fin positions in relation to airbrakes, and yaw positions. Table 1 gives a provisional view of these configurations.

*Table 11 - Test Configurations*

Test Configuration	Fins	Air brakes	Tufts	Yaw	Extra features
1	off	stowed	no	no	-
2	off	stowed	yes	no	-
3	on	stowed	no	no	-
4	on	stowed	yes	no	-
5	on	stowed	yes	1 degrees	-
6	on	stowed	yes	2 degrees	-
7	on	stowed	yes	3 degrees	-
8	on	stowed	yes	4 degrees	-
9	on	deployed	yes	no	Vary airbrake deployment extent
9	on	deployed	yes	no	Fins aligned with airbrakes
10	on	deployed	yes	no	Fin/airbrake alignment setting 1
11	on	deployed	yes	no	Fin/airbrake alignment setting 2

#### 4.2.3.4 Review of Previous Testing

In previous testing, several factors limited the team's ability to acquire meaningful results. Issues with the manufacture and performance of the model itself caused delays and time spent fixing issues. A priority of this round of testing is to have a high-quality model, helping to minimize any time wasted during our tunnel testing week. Thorough design and careful manufacture allowing for adequate time to complete each step should help towards this goal. Another improvement was speeding up changes between configurations. Designing to a higher level of modularity will aid this. Data acquisition, storage and processing posed another challenger in previous testing. Therefore, adequate time, research and work shall be dedicated to the development of the data acquisition system, allowing for smoother

operation during testing and easier post-processing. The methods to acquire flow field data shall also be reviewed. Although tufts were previously used, a camera-based method to properly visualize and track these should be developed and implemented.

#### 4.2.4 Wind Tunnel Model Design

The previous model itself had structural design flaws. In particular, the 3D-printed airbrake assembly disrupted the structural integrity of the stringer-based spine, resulting in bending moments through the model. This caused the nose and rear end to sag. Section 5 explores some initial design concepts for various parts, implementing some improvements on the shortcomings of the previous model design. Some key requirements behind the design of this new model are modularity and adaptability. It shall be used to aid the development of the rocket's aerodynamic design over several years, so the ability to change key parameters such as length and diameter is essential. Also, it must be robust and manufactured to a high quality, to allow for this longevity.

*Table 12 - Design option trade-off matrix*

Design Feature		Design option 1			Design option 2	
		Advantage	Disadvantage		Advantage	Disadvantage
Main Skeleton	Bulkheads with stringers	-Good load transfer -Easy attachment of panels -Modularity	-Very little room between stringers -Stiffness could be improved	Bulkheads with central rod	-Superior stiffness -Simple integration -Room around central rod	-Need load transfer pathways -Difficulty machining – all attachment points must be precisely drilled perpendicular. -Panels require standoffs
Fin can	Modular slip-on steel core fins	-Variability in number of fins -Steel cores adaptable to multiple fin designs	-Very heavy -Routing of pressure tappings can be challenging	Clamshell 3d-Printed fins	-Lighter, less complex -More internal space	-Non-modular

##### 4.2.4.1 Spine

One of the key aspects of the spine design which shall be reviewed is stringers. L-profile stringers were used in the previous model, demanding complex, purpose-designed joggles and adapter pieces in order to fix the external panels securely onto the spine. A more suitable profile would be a C-type (Figure 36). This brings benefits both from a structural and practical perspective; a flat outer surface will allow for easier attachment of panels compared to the L-profile. Another option under consideration is a cylindrical tube (Figure 37), from which stand-offs will be fixed, allowing for panel attachment. A redeeming feature of this design would be ease of access around the spine, which was a hinderance of the stringer-based design. It was difficult to fit tools and pressure looms between each stringer. A tube featuring adapters and stand-offs would remove this problem. Also, this would make the design more adaptable. With the height of the standoffs adjustable to allow for different circumferences, the model can change as the design changes over time.

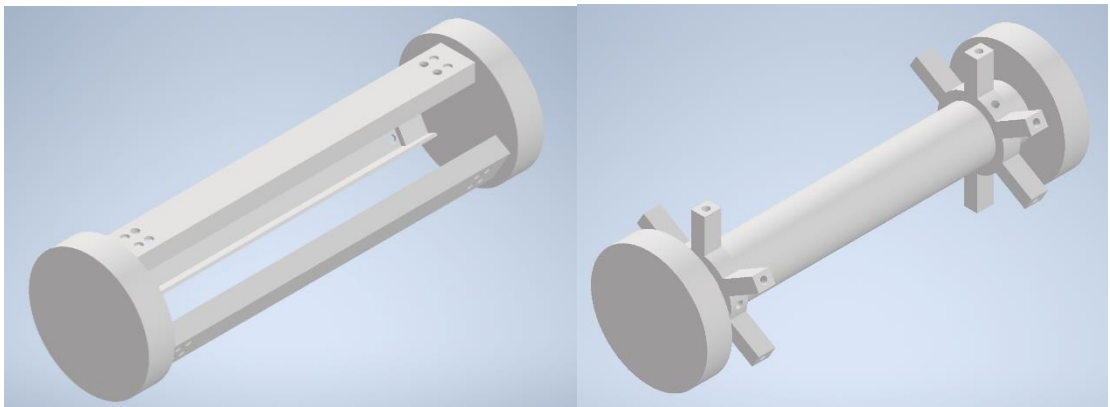


*Figure 36: C-Section*

*Figure 37: Central Tube*

#### 4.2.4.2 Mounting Section

A significant requirement that this model needs to fulfil is being very stiff. To achieve that, many parts of the model will be made from metal, increasing the weight of the rocket. Thus, the wind tunnel mounting mechanism will have to be very robust and stiff. The mounting section would also have the advantage of being modular, i.e. it could easily be transferred along the rocket, enabling us to accommodate for changes in the position of the centre of gravity.

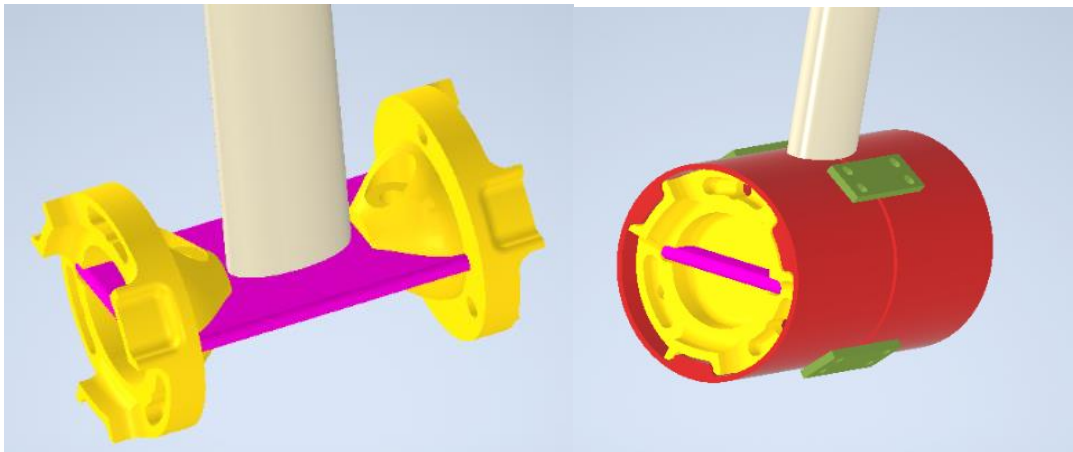


*Figure 38 : Tunnel mount*

The WT strut (white) will terminate in a welded plate which we will bolt onto our own plate (magenta) and sandwich between two bulkheads with bolts fastening them together for better load transfer. The issue with this approach lies in the fact that we will not be able to assemble the entire model without integrating the strut beforehand. However, this method provides a large area for load transfer.

A different approach to the problem would be to instead have the plate that strut terminates at only bolt to the magenta plate and not interfere with the bulkheads. That would reduce the assembly required after placing the strut in place. The entire section will be enclosed by two halves of a tube (red) that have a cutout for the spar and are held together with adapters (green). The external tube will have extrusions on either end that slide into grooves in the bulkheads to help transfer the loads effectively. Potential issues of this design would be access for fastening the bolts to adjacent sections.

A slightly different idea would be to have the external tube cut horizontally into three parts and bolted perpendicularly into the bulkheads while using adapters that curve along the diameter. This way they could easily be assembled last when putting the model together. This issue here is the cuts will be made

along the length of the tube which is the main load path, so some of the stiffness that the tube provides will be lost.

#### 4.2.4.3 Nose Cone

The requirement for this nose cone design was to have minimum drag. The design is based on the Von Karman shape. This is a modified elliptical shape that minimises drag at higher speeds. The length of the nose cone is 320mm with a radius of 50.75mm which are the dimensions for the half scale wind tunnel model. A cylindrical extrude of 35mm is added to the end of the nose cone to ensure mounting to the rest of the rocket.

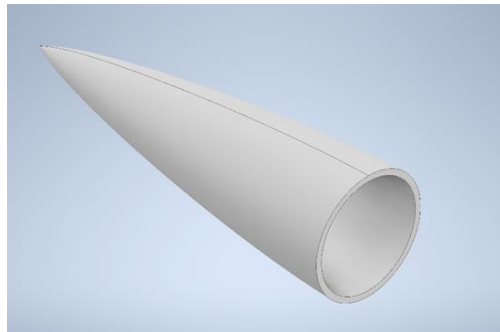
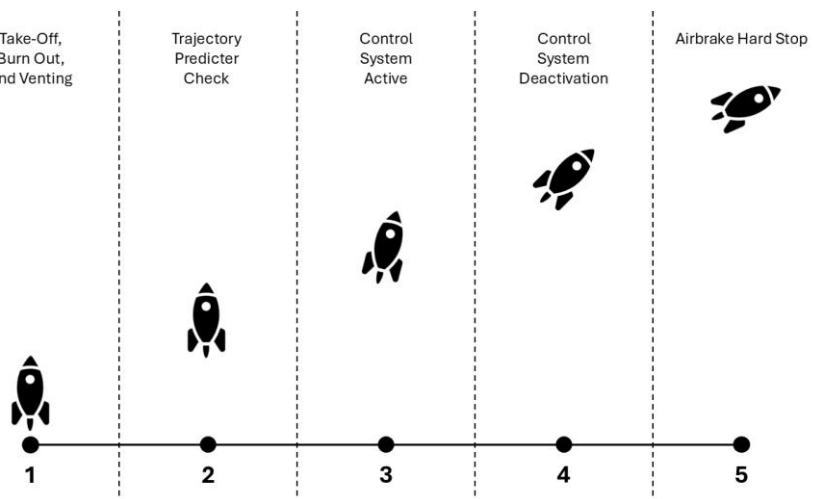


Figure 39: Nose cone

## 4.3 Controller design

## 4.4 Controller Design

### 4.4.1 Control System Concept of Operations

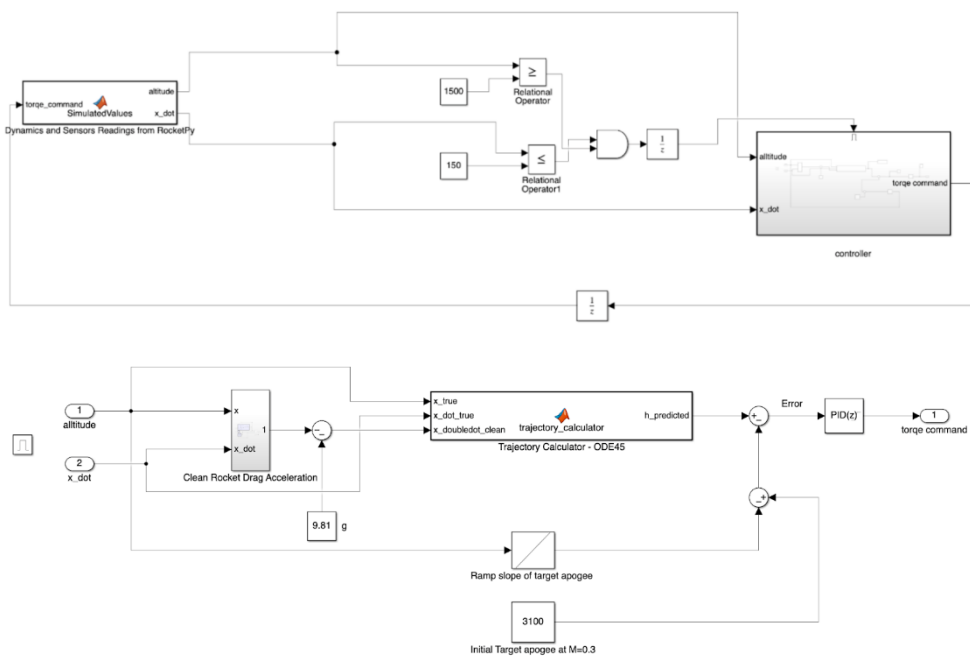


The overarching aim of the control system is to allow the rocket to reach the target apogee of 3000 meters. This is achieved by designing the clean rocket to achieve a higher apogee to prevent undershoot and then deploying the airbrakes to slow the ascent as necessary to reach the target. The overall Concept

of Operations of the control system is illustrated in Figure XX, with a written description of the stages provided below:

1. Take-Off and Burn Out
  - During the burn, the control system will not be active.
2. Trajectory Predictor Check
  - After burn out, the rocket will enter the coast phase, where the rocket will have constant mass and predominantly experience drag and weight forces. At this point the trajectory predictor will be activated, using the current altitude and speed to predict the rocket apogee, however the airbrakes will remain inactive and mechanically locked. To check for error, the trajectory predictor will predict the altitude in 5 seconds time. Once these 5 seconds have passed, the predicted and actual altitude will be compared and the resulting error will be incorporated into future apogee predictions through extrapolation. This should allow the control system to deal with any systematic error within the trajectory predictor.
3. Control System Active
  - Once the rocket has surpassed 1500m altitude and is below 150m/s the airbrake mechanical lock will be removed and they will be deployed to slow the rocket as needed.
4. Control System Deactivation
  - At any point after the rocket passes 2950m, if the predicted apogee is within 10m of the target the control system will be deactivated, and the airbrakes stowed and mechanically locked.
5. Airbrake Hard Stop
  - If the rocket reaches the target apogee of 3000m with a vertical velocity greater than 0m/s, the airbrakes will be fully deployed to slow the rocket as quickly as possible. Once 0m/s vertical velocity is reached the control system will be deactivated, and the airbrakes stowed and mechanically locked, allowing for a safe descent of the rocket. The case of the airbrakes not properly stowing is not of concern, as the location means they will not interfere with the recovery system (parachutes).

#### 4.4.2 High Level Overview



A feedback controller will be used to facilitate disturbance rejection, improve dynamic adaptability and contain the rocket to a recovery-capable flight envelope. The PID-based controller is initially supplied with a high setpoint, which is gradually scaled down to the intended target apogee of 3 kilometres using a ramp slope. The setpoint is compared with the projected apogee extrapolated by the trajectory predictor (described in Section 4.4.2.3) based on feedback sensor values on current altitude and vertical velocity, generating an error signal. The error signal is fed into a PID controller to generate an air brake actuator command, simultaneously driving all three servos to the required deployment angle. Figure XX shows the overall system diagram, and the implemented logic for Stage 3 of the Concept of Operations. Figure XX presents the controller block, including the trajectory predictor and the PID controller.

#### 4.4.3 Trajectory Predictor

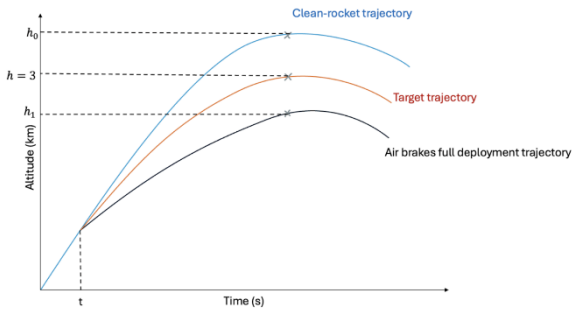
Measured values of altitude, velocity and brake drag coefficient are used as inputs for the Simulink model. Currently, these values are supplied using Rockepy to simulate the rocket's launch but in future and for the launch they will be taken from direct telemetry on the rocket. From these values, the clean rocket drag, and airbrake drag can be calculated using the drag equation. Summing this drag with the rocket's gravitational acceleration provides the overall deceleration (acceleration towards the earth) of the rocket. This acceleration, as well as velocity and altitude all feed into the ODE45 Trajectory Calculator block. The ODE45 block effectively solves differential equations and uses the input values to predict the altitude and velocity of the rocket over a range of 50-time steps. The maximum value reached by the altitude is then assessed and output as the predicted apogee of this trajectory, or `h_predicted`. This is what the Simulink controller then uses to judge current error and whether airbrakes need to be applied.

#### 4.4.4 Envelop Controller

A simple guidance algorithm was developed as a back-up ‘controller’. It relies only on the instantaneous measurements of the sensors and can be used in case of faults in the main controller. Once Stage 3 of the flight is reached the ‘controller’ becomes active. The trajectory predictor detailed in Section XX will be used and if the maximum altitude of the clean-rocket (without air brakes) exceeds the target of 3km the guidance will get activated. Based on the instantaneous prediction the flight envelope will be calculated for the two ‘edge cases’ of full airbrake deployment and clean-rocket and the maximum altitude in both cases will be recorded. Then, Equation X will be used to determine the percentage of deployment of the air brakes, where  $h_0$  is the clean-rocket maximum altitude,  $h_1$  is the maximum altitude that could be reached if the air brakes are fully deployed,  $h = 3$  km is the target altitude, and  $x$  is the required air brakes deployment in percent. The expression derived for Equation X realises a linear interpolation between the cases of 0% and 100% air brakes deployment. Figure XX shows the scenario, where  $t$  is the current moment in time. The same calculation repeats at all time steps until the target (the frequency has not been determined yet).

$$x = \frac{h_0 - h}{h_0 - h_1}$$

Equation (X)



Analysing this alongside previous launch data, avionic component specifications, and consideration of command propagation to system response latency - a decision has been made to limit the final controller frequency to 50Hz

#### 4.4.4 PID Controller Tuning of Gains

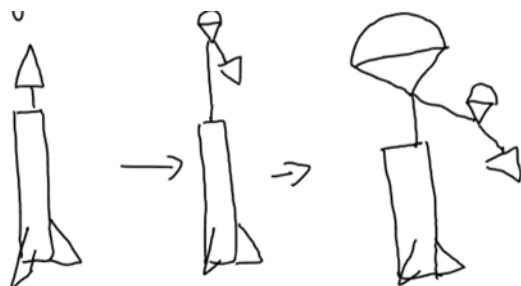
The purpose of the PID controller is to act as a further ‘fine tuner’, provide greater disturbance rejection, adding robustness and allow the system to cope with the ramped reduction of reference setpoint. Multiple iterations are being computed with varying input signals to identify a maximum allowable steady-state error as a factor in our selection of the Proportional gain, KP, of the PID controller. Derivative gain, KD, will be used to minimise any significant oscillatory behaviour that has not been filtered by the transfer function. Methods will be taken to prevent susceptibility to noise.

To tune the controller, we need the drag coefficients from wind tunnel testing. However, since this won't be available until later in the design process once the wind tunnel testing is completed, initial testing of the simulation, controller, and tuning method was performed by assuming flat plate drag for the airbrakes,  $C_d = 1.28$ , across all deployment levels and Mach numbers. This was deemed a reasonable initial assumption since we also assume the rocket will not exceed Mach 0.3, thereby staying in the incompressible flow regime where flat plate drag is valid. During the simulation in RocketPy, the additional drag from the airbrakes is then calculated using the reference area \* deployment level, Mach number, and density.

#### Rocket Recovery

##### Single separation dual deployment:

The chosen method for recovery is a single separation dual deployment, this consists of a removable nose cone and a charge ejecting a smaller drogue parachute before the main parachute gets released.



This is easier on the design of the rocket as only one section needs to be removable as well as allowing for a drogue parachute to be released earlier controlling the decent

### Ejection method:

In recovery there are a few main types of ejection methods with the main ones being black powder and CO<sub>2</sub>, in the past black powder has been used but significant damage to the parachute lines made it desirable to make a switch to CO<sub>2</sub>.

Criteria		Reliability	safety	age/reusability	size and weight	cost	reaction loads	deployment	Total	%
	X	1	2	3	4	5	6	7		
Reliability		X	3	3	9	3	3	3	24.00	27
safety	1		3	1	3	3	3	3	13.33	15
damage/reusability	2	0.333333	X	1	3	3	3	3	13.33	15
size and weight	3	0.333333	1	X	9	3	3	9	25.33	28
cost	4	0.111111	0.333333	0.111111	X	1	0.333333333	0.111111	2.00	2
reaction loads	5	0.333333	0.333333	0.333333	1	X	0.333333333	0.333333	2.67	3
deployment	6	0.333333	0.333333	0.333333	3	3	X	1	8.00	9
	7	0.333333	0.333333	0.111111	9	3	1	X	13.78	15
		1.78	5.33	4.89	34.00	16.00	10.67	16.44	89.11	100
		2.0	6.0	5.5	38.2	18.0	12.0	18.5	100	89.11

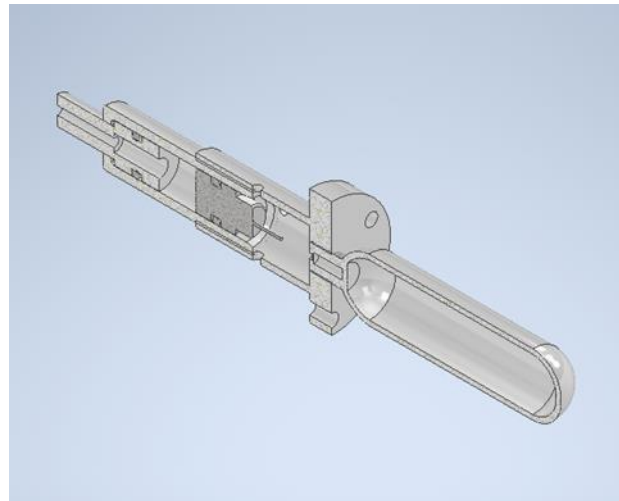
Consideration was given to the different design criteria and they were ranked in a pairwise comparison matrix. The most important factors needed to be considered in our design were reliability, to ensure parachute is ejected and safety to protect people and the rocket.

CDA matrix										
Criteria	Weightings	Designs →	Black powder	CO <sub>2</sub>	Spring	slug gun	tractor rocket	smokeless powder		
			score	weighted score	score	weighted score	score	weighted score		
reliability	0.270	1	4	1.1	3	0.8	4	1.1	2	0.5
safety	0.150	2	3	0.5	5	0.8	3	0.5	3	2
damage/reusability	0.280	3	3	0.8	5	1.4	5	1.4	4	1.1
size and weight	0.030	4	3	0.1	2	0.1	4	0.1	2	0.1
cost	0.030	5	4	0.1	2	0.1	3	0.1	2	0.1
reaction loads	0.090	6	2	0.2	2	0.2	4	0.4	3	0.3
deployment time	0.150	7	5	0.8	5	0.8	2	0.3	3	0.5
			Total score for design →	3.5	4.0	3.8	3.0	1.6	3.2	

Considering the different ejection methods for parachutes and ranking them against the criteria the preferable method was found. CO<sub>2</sub> came out on top but by a small margin, since the mass of spring required to create enough force to eject the parachute would be very large and the safety concerns around spring as they are always compressed and armed CO<sub>2</sub> seemed the best choice.

### CO<sub>2</sub> subsystem:

The black powder will be ignited creating a charge causing the puncture piston to inject the CO<sub>2</sub> canister, which will in turn release the parachute. The next steps for this will be refining the initial concept to integrate into the rocket design from last year to visualise how it will all come together.



### Load through parachute line

Calculations show that the load through recovery line after parachute deployment

$$= 89.4 \text{ kN}$$

This is the load through the main parachute line disregarding the effect of the drogue parachute with values estimated from last years rocket values. While this force seems high it is the initial force after parachute deployment and will begin to reduce with a lower force through line. Next steps in calculation would be to calculate the ejection force of the parachute, which is in the works and total force on lines with consideration given to the drogue parachute.

**10 Pages for Launch Vehicle**

## 6. Ground Operations

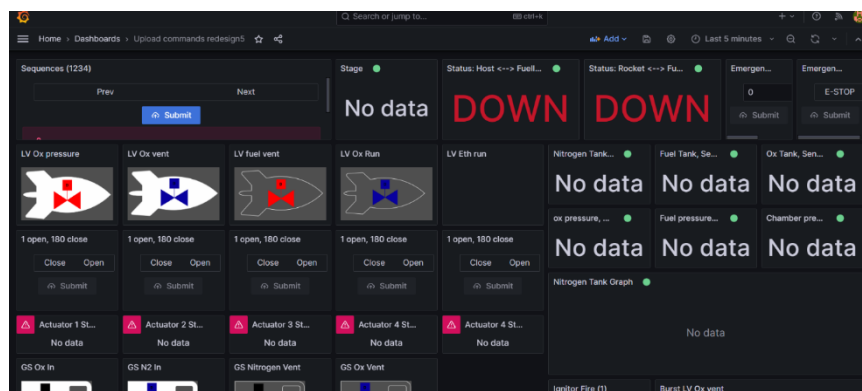
### 6.1 Mission Control

The connection between the fuelling cabinet and mission control is facilitated through point-to-point Wi-Fi (PTP), which last year has been successfully tested up to 800m. There are two communication links between mission control and the vehicle: a LoRa link predominantly used during flight, and an indirect CAN channel interfaced through the local Wi-Fi network. This redundancy enhances the resilience of mission control communications.

#### 6.1.1 Software

Mission control serves as the central hub where all data feeds converge, allowing for the control and monitoring of sub-systems on both the rocket and the fuelling station. Building upon last year's design, it hosts two primary services, packaged as Docker containers for ease of interchangeability and initialization: a user interface and a backend API. These services enable the team to view live data through a streaming service and provide remote-control capabilities for fuelling operations.

This year, the dashboard will be enhanced using the Canvas plugin in Grafana to create a more intuitive and visually appealing interface. Each valve and pressure reading will be individually labelled and clearly always displayed. Additionally, there will be a transition from the current use of MQTT brokers to MQTT over WebSocket, simplifying the communication architecture and enabling a cleaner Piping and Instrumentation Diagram (P&ID). Prototypes for the new UI and the necessary WebSocket wrappers around the brokers are currently being developed. The [Figure X](#) below, from the last design cycle, is undergoing updates to reflect these changes.



#### 6.1.2 Hardware

The electronic system for ground systems is divided into two main cabinets. The first houses the power sources: a backup battery and a 230VAC mains to 15VDC PSU. The two power sources are connected through ideal diodes, which enable seamless power transfer in case of a mains power loss. Since the mains PSU voltage is higher than the battery (15V vs 13Vmax), power will not be drawn from the battery during normal mains operations.

The second (main) cabinet contains the ground system control electronics and power regulation components required to create the necessary power rails. Panel mount connectors facilitate the transfer of power and data through the cabinet. A Raspberry Pi and Ground Station Control Unit form the main control electronics of the ground station. The Pi manages ground operations and communicates over CAN, and connects to mission control through an Ethernet link to the PTP Wi-Fi

network. The GSCU communicates with the Pi over CAN and control servos, and senses current draw and pressure transducers. 5V rails power the exhaust fan, GSCU, and Pi. A BEC creates the 7.4V needed for the servo valves, and a buck-boost converter generates 12V to power the pressure transducers. A 24V converter is used for the PoE Wi-Fi injector, and 18V is generated to charge the on-board batteries in the rocket and provide ground power.

Additionally, there is a weather resistance air inlet to allow airflow over electronics. Component power loss and reliability were prioritised over size and weight.



## 6.2 Remote Fuelling Operations

### 6.2.1 Feed Systems

The plumbing and instrumentation diagram for the GS is shown. A focus was to create the bare minimum system to allow safe fuelling operations. See Appendix for the fuelling operation details.

With the failures last year, it was impossible to use the GS to fuel operationally and hence the lessons learned were limited. Nonetheless, there have been some design changes, most notably the presence of a pump and quick disconnect on the ethanol line that now allows for complete remotely operative functionality.

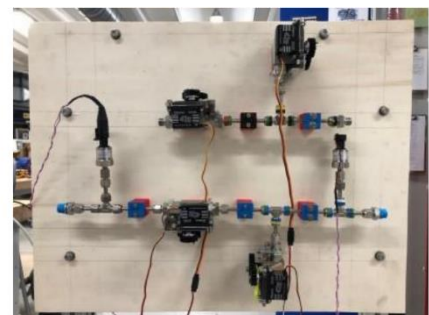
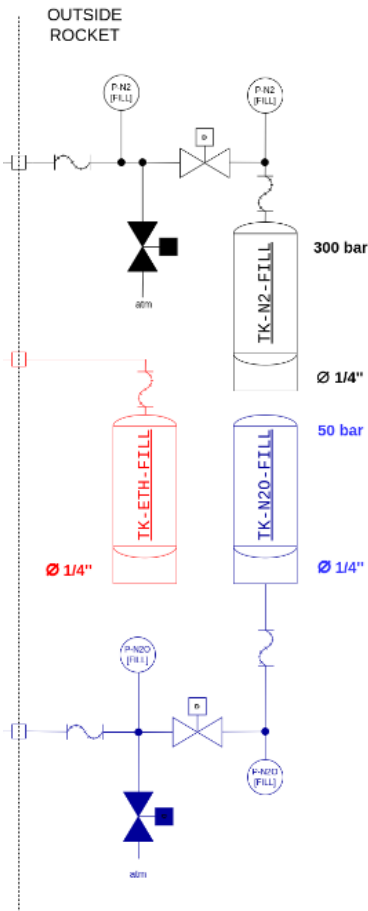


Figure 41 Ground station electronics box and plumbing panel

Figure 40 P&ID of the ground station

### 6.2.2 Fuelling Operations

Figure X outlines the operational sequence of actuated valves during the fueling process for a rocket. Each valve is individually controlled, except during an emergency stop (e-stop), which automatically vents the rocket tanks to ensure safety. The ground station and rocket share a consistent valve safety protocol. During nitrous oxide filling, the rocket's vent valve operates under P&ID control,

transitioning to rocket control once the tanks are filled. The sequence involves opening and closing specific valves to manage fuel flow, culminating in the disconnection of fueling lines and preparation for launch. This structured approach ensures a controlled and safe fueling process, with clear stages and a reliable emergency protocol.

Stages/ Parts	F_N2O_pValve	F_N2O_ventValve	G_N2O_inValve	G_N2O_ventValve	G_N2_inValve	G_N2_ventValve	F_Eth_ventValve	F_N2O_outValve	F_Eth_outValve
1.1	CLOSED	CLOSED	CLOSED	CLOSED	CLOSED	CLOSED	CLOSED	CLOSED	CLOSED
1.2	CLOSED	CLOSED	CLOSED	CLOSED	CLOSED	OPEN	CLOSED	CLOSED	CLOSED
1.3	CLOSED	CLOSED	CLOSED	CLOSED	CLOSED	CLOSED	CLOSED	CLOSED	CLOSED
Open cylinder valves									
Leave launch pad									
2.1	CLOSED	CLOSED	CLOSED	CLOSED	CLOSED	CLOSED	CLOSED	CLOSED	CLOSED
2.2	CLOSED	CLOSED	CLOSED	CLOSED	OPEN	CLOSED	CLOSED	CLOSED	CLOSED
2.3	CLOSED	CLOSED	CLOSED	CLOSED	CLOSED	CLOSED	CLOSED	CLOSED	CLOSED
3.1	CLOSED	CLOSED	OPEN	CLOSED	CLOSED	CLOSED	CLOSED	CLOSED	CLOSED
3.2	CLOSED	CONTROLLED	OPEN	CLOSED	CLOSED	CLOSED	CLOSED	CLOSED	CLOSED
3.3	CLOSED	CLOSED	CLOSED	CLOSED	CLOSED	CLOSED	CLOSED	CLOSED	CLOSED
4.1	OPEN	CLOSED	CLOSED	CLOSED	CLOSED	CLOSED	CLOSED	CLOSED	CLOSED
4.2	CLOSED	CLOSED	CLOSED	CLOSED	CLOSED	CLOSED	CLOSED	CLOSED	CLOSED
4.3	CLOSED	CLOSED	CLOSED	CLOSED	OPEN	CLOSED	CLOSED	CLOSED	CLOSED
5	CLOSED	CLOSED	CLOSED	CLOSED	CLOSED	CLOSED	CLOSED	CLOSED	CLOSED
Disconnect fuelling lines									
6	CLOSED	CLOSED	CLOSED	OPEN	CLOSED	OPEN	CLOSED	CLOSED	CLOSED
Launch (ground station hands permission of valves to rocket)									
E-STOP	OPEN	OPEN	CLOSED	OPEN	CLOSED	OPEN	OPEN	CLOSED	CLOSED

### 6.2.3 Quick Disconnect Mechanism

The Quick Disconnect (QD) allows the launch Vehicle to make a secure seal with the fuel lines on ground, be fuelled and then be remotely be disconnected allowing for a safe fuelling of the launch vehicle. In compliance to the EuRoC Design Requirements and conforming to the design of the BSEP Engine design, there are two dissimilar QD connections for the Fuel and Oxidiser lines respectively. The decision was made to use COTs QD couplers which would be released using a custom, SRAD release mechanism. The Couplers were chosen to meet the following criteria:

Fluid	Sealing Pressure (Bar)	Minimum Temperature (K)
Nitrous, N2O		
Ethanol + Water		
Nitrogen		

The prototype version as of 1<sup>st</sup> of February 2025, involves a two-part mechanism; a static housing for the coupling and the servos and a dynamic sleeve around the head of the QD which retracts (using the servos). The servos have cams which slot into the sleeve to aid the same. The following diagram highlights the mechanism.

To test the Quick Disconnect, a test plan was made with entry and exit criteria was made. The aim with the quick disconnect was aimed at being able to function in a partial failure state (eg. Failure of one servo) and increased reliability (reduced chance of failure). Refer Testing annex.

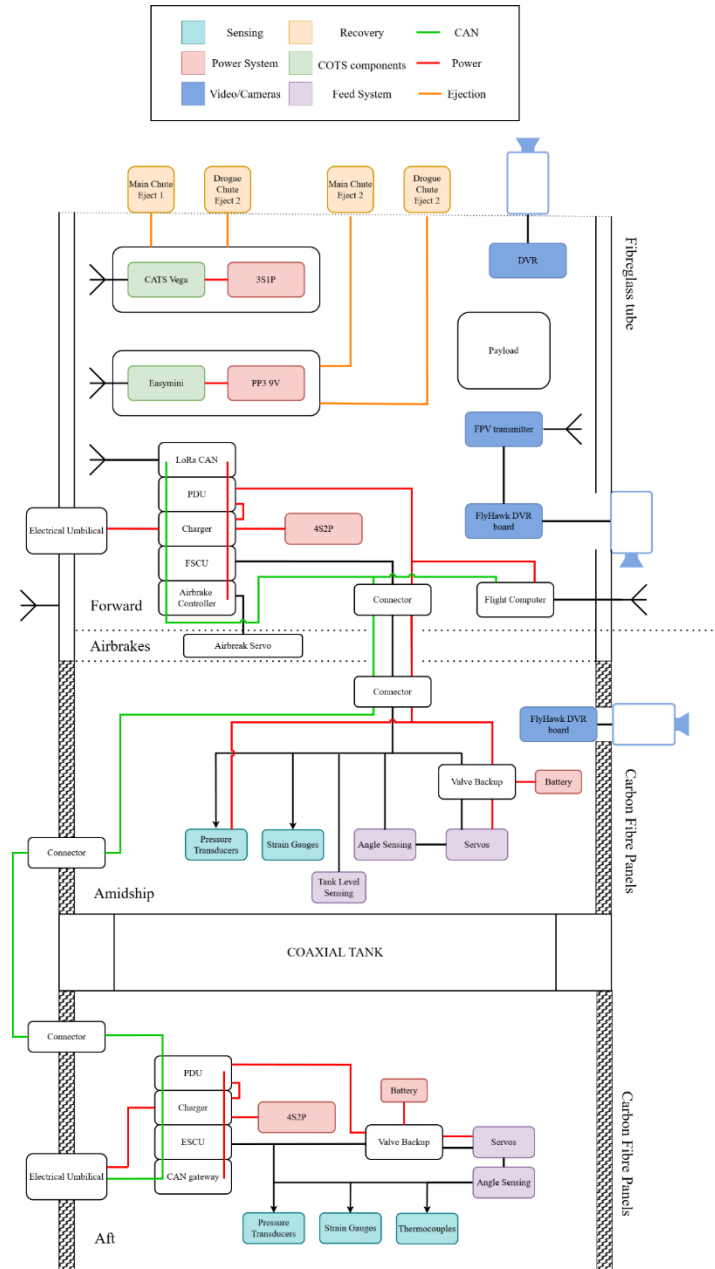
# 7. Avionics

## 7.1 Avionics overview

Project Waxwing's avionics system iterates on Project Feynman's architecture. This includes refining board position and placement through converting it to a physical stack, adding improvements to each board and adding the ability to control recovery. The avionics is split into two main categories, comprising of COTS boards and the SRAD system. The COTS boards are used for redundant recovery, and a camera system, which allows real-time monitoring of vents and airbrakes.

The SRAD electronics run the engine and airbrakes through two 4S2P 18650 li-ion based battery packs, through a charger controller and power distribution unit. A CAN bus is utilized to transfer data between all boards in the system and the ground station. This is realised through a magnetic umbilical connection, which provides charging capacity for the batteries, and a gateway board during ground operations. A LoRa board transmits data during flight and recovery and can receive commands in case of an off-nominal flight.

The development plan for Project Waxwing is split into two boards per developer, for hardware and software. The first cycle includes the Feed Systems Control Unit, Valve Backup Board, Charging Board, LoRa Board, Flight Computer, and CAN gateway, to be ready by the start of February. The second cycle consists of the Engine Control Unit, Power Distribution Unit, LoRa ground, Flight Computer Ground, Airbrake Controller and Airbrake Backup Board, which will start development in February and will be completed in March. The boards will be sent for manufacture in early March, with debugging and testing of relevant boards to be completed by the April subscale launch.



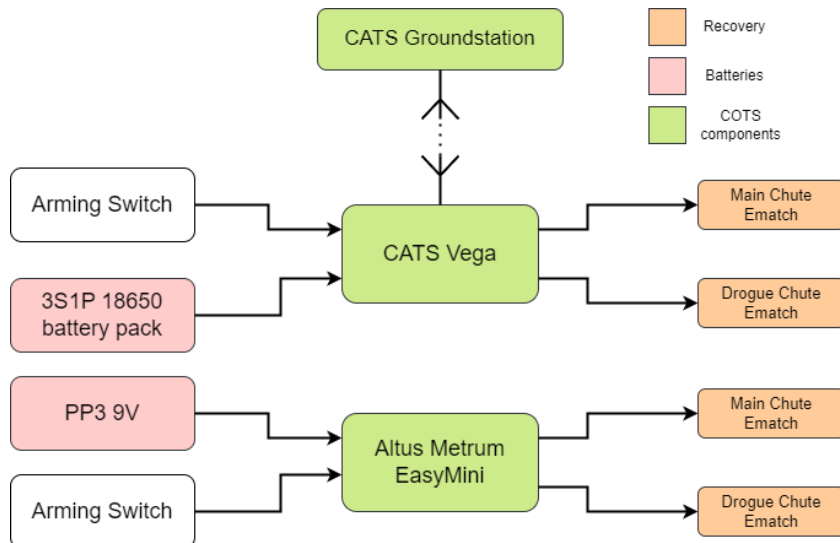
## 7.2 COTS avionics system

### 7.2.1 Recovery

The system uses a CATS Vega and an Altus Metrum EasyMini to ensure a redundant recovery system. The CATS Vega is powered by an isolated 3S1P 18650 battery pack, which allows for 36 hours of operation time. The EasyMini is powered by a PP3 9V battery, which has been proven on multiple test flights to be a reliable power source for e-match ignition. This battery allows for 25 hours of operation time.

Component	Max current consumption (mA)	Voltage input (V)	Calculated battery life (h)
CATS Vega	1000	7-24	36
Altus Metrum EasyMini	20	3.7-12	25

Component	Capacity	Voltage (V)
3S1P 18650 Battery Pack	3600	9.6-12.6
PP3	500	9



### 7.2.2 Camera System

The camera system utilises two Hawkeye Split V5 4K FPV camera systems, one RunCam Mini FPV DVR and a Holybro Atlatl HV Micro video transmitter. These are wired onto the main power bus, and give footage of stage separation, airbreak actuation, and a side view.

Component	Max current consumption (mA)	Voltage input (V)
Hawkeye Split	300	7-28
RunCam Mini DVR	250	3.3-5.5
HolyBro Atlatl FPV transmitter	300	5-23

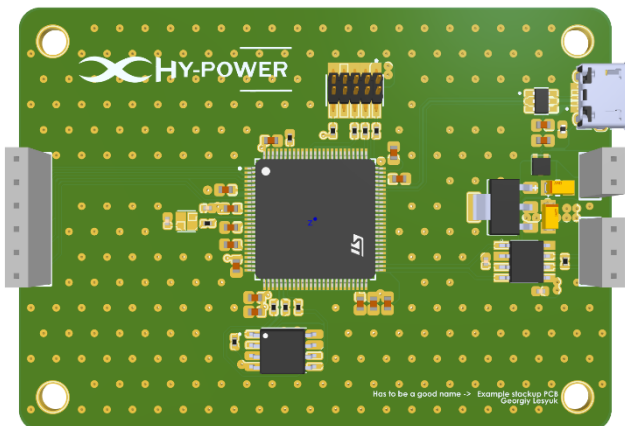
## 7.3 SRAD hardware

### 7.3.1 SRAD avionics overview

The SRAD avionics system is developed around the STM32 series of microcontrollers. This was chosen because of the versatility of these chips, vast documentation and support, and previous experience with software development and debugging.

The boards are concentrated in two flight stacks, to reduce the amount of wiring, complexity in mounting, and to assist testing without the launch vehicle. The forward stack is responsible for LoRa transmission, airbrake control, and feed systems control. These boards will carry out the PID controller for the airbrakes, and the feed systems' open-loop controller. The aft stack is responsible for CAN transmission to the ground station, and engine control via the open-loop controller. Both stacks rely on their own 4S2P battery source.

### 7.3.2 [unnamed] hardware template

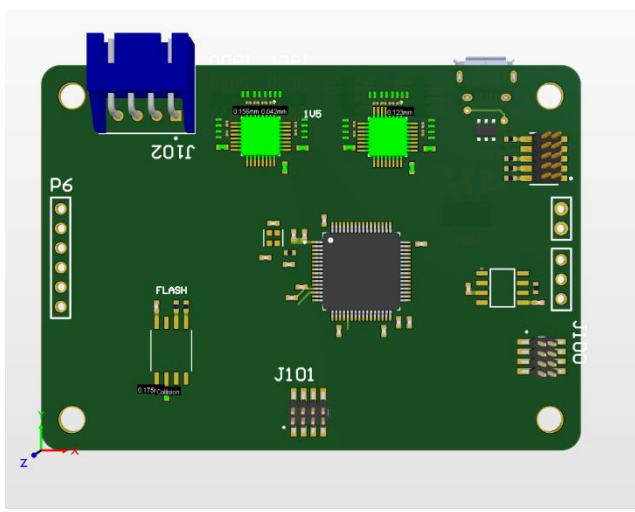


Dimensions [mm]	50x70
GPIO pins	6
Voltage In	5V
CAN 2.0 Channels	1

All boards use the [unnamed] schematic and layout template for use within the system. This template standardises key components used in the system as well as layout positions, which is critical within a stacked board structure.

Standard parts include LDOs for power conversion to the MCU's 3V3 required voltage, a CAN transceiver for the launch vehicle's CAN 2.0 bus, W25Q128x 16Mb flash memory for data logging, connector for debugging, headers and USB connections and peripherals. This assists the team by ensuring that there is a strong foundation to build upon, and to keep back up stock of common components in case of board failures. Six GPIO pins were included in the system to aid various external functions which were desired in the previous cycle, such as controlling cameras and transmission.

### 7.3.3 FSCU



Spec	Quantity
Configurable PWM/ADC input channels	8
Wheatstone Bridge ADC channels	24
I2C Interface	1
High Current (15A) Ammeters	8
Low Current (30mA) Ammeters	8
PWM output channels	8

The Feed Systems Control Unit will provide plumbing control and monitoring above the coaxial tank, with interfaces for 8 servo valves (PWM control, Angle feedback and current meters), 8 current type pressure transducers and 24 strain gauges across 8-12 rosettes for structural monitoring.

Most interfaces are conducted through 5 ADS131M08 ADC chips with some going into the MCU, a STM32F412GT6. Due to the large number of differential strain gauges channel inputs, a high pin density header was needed to fit them onto the board footprint. The Angle Sensor interfaces are configurable between analog, PWM and I2C types to allow for a choice between simple potentiometers or digital rotary encoders. The ammeters are designed with current sense resistors, for which the servo ammeter resistors are to be placed off-board due to size and current requirements.

The FSCU's primary function is to realise PID control of servo motors by providing PWM output. The duty cycle of the board is updated at a provisional rate of 1khz, and the data by which the required duty cycle is set is received via the ADCs. The chips are synchronised by an initialisation function and are sequentially read whenever the data-ready signal is given. This board employs DMA, and the MCU receives commands and sends data over the CAN bus at a provisional rate of 2hz. The MCU stores a subset of the data to W25Q128x flash at a rate of approximately 5hz so as not to overflow the memory. Due to the low data rate required, the decision was made to transition from a Dual SPI to standard SPI interface.

#### *Magnetic Angle Encoder*

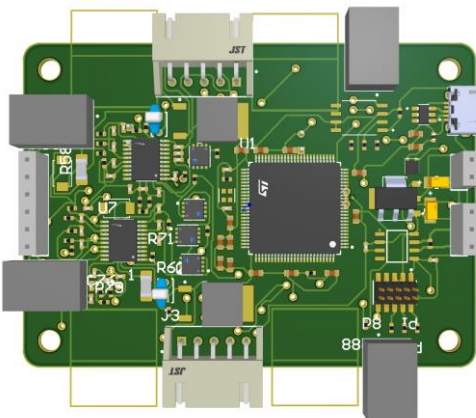
This under-development board will provide a more sophisticated alternative for angle sensing to the currently planned potentiometers using hall effect rotary encoder chips such as the A1335.

### 7.3.4 Valve Backup Board

All feed system valves will have an electronic backup board. The board will provide a set PWM signal from a 555 timer that can be trimmed as required. When PWM from the actuator board is lost, a transistor-based circuit will allow the redundant PWM generated by the 555-timer circuit to pass through to the output terminal for the servo. There will be 2 variants of the board depending on whether the failsafe position for the valve is open or closed.

The valve backup provides redundant power via its own cell, regulated to 7.4V with a power load switch that will automatically draw from the cell when main bus power is lost.

### 7.3.5 Charging board

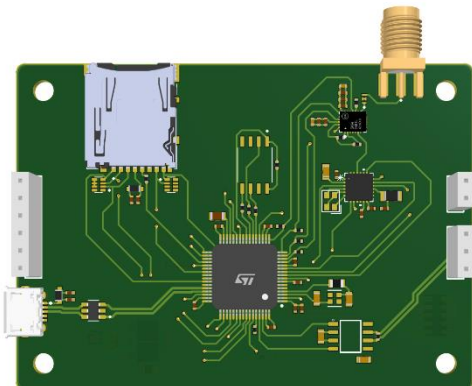


Input Voltage [V]	18
Output Voltage [V]	12.8-16.8
Battery Charging	4S2P
Sensing	Voltage, Temperature, Current

The Charging Board is based around the BQ24616RGER chip by Texas Instruments, which can charge a 1-6S li-ion battery pack, as well as offering input overvoltage protection, temperature control, battery overcurrent and overvoltage protection. The BQ2461 has power path switching to ensure that the batteries are not getting discharged simultaneously while charging. This charging chip is been paired with the BQ7692006PWR chip by Texas Instruments which acts as a Battery Monitoring System (BMS) which ensures that all the cells in the battery pack are uniformly charged by regulating the current flow in each cell. The charging chip receives 18V from the ground station and supplies 16.8V to the BMS to charge the 4S battery pack. The board sends real time voltage monitoring and precise charging control via CAN. The batteries used are Panasonic NCR 18650B 3.4Ah Li-ion cells, in a 4S2P configuration, which provides a 16.8V 6.8Ah battery pack.

Battery charging enabling/ disabling is operated by a signal transmitted by the microcontroller, through two GPIO pins connecting to each of the two 4S battery backs. These chips are communicated with via independent I2C buses to retrieve information from status registers which software translates to cell voltage levels, pack current and pack temperature. This information will be sampled at a provisional rate of 1Hz and stored to a W25Q128x flash chip using SPI alongside being transmitted to the ground station over the CAN bus. Each BMS chip comes with a dedicated ‘ALERT’ GPIO pin to send an interrupt signal to the host microcontroller, for example due to the occurrence of a fault event. Fault events and error states will also be logged and communicated over CAN.

### 7.3.6 LoRa



Input	CAN LoRa
Output	CAN LoRa

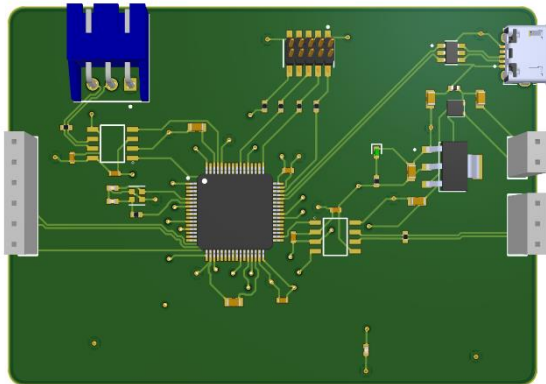
LoRa communication is handled by two boards: LoRa onboard and LoRa ground.

The LoRa onboard utilises an STM32F412RET6 MCU to enable interfacing between LoRa and external systems. The board contains a CAN connection, 6 GPIO pins, a Micro USB connection and an ability to store data to SD. Specific LoRa components include a 2.4GHz SX1280 LoRa transceiver and an SE2431L front-end module. LoRa transceiver communicates with the MCU via SPI.

The onboard software has the following functions: receive CAN messages from the ground and transmit them to the bus, process CAN messages and transmit them to the ground, ascertain if there is no data from a board and transmit this information, transmit a heartbeat every second, and log all transmitted information to an SD card

To perform all these tasks at consistent intervals, FreeRTOS handles the task scheduling. The task priorities are given that of the order above; if over a second has passed since the board last transmitted a heartbeat, that will be given priority over logging to the SD card. Communication to the LoRa chip (SX1280) is handled over customized SPI drivers; Semtech's provided drivers are in C++, incompatible with the embedded C used for the rest of the code. CAN FIFO interrupts are used to handle and send each message to the chip.

### 7.3.7 CAN Gateway



CAN I/O buses	2
Flash chips	4
Storage types	SD/Flash

The board is based around the STM32H523RCT7 microcontroller, as this has the necessary CAN FD, SDMMC and QSPI connectivity options. The two CAN gateways are MCP2562T-E/SN chips, which provide CAN communication at up to 1Mbps, which is more than sufficient for this application. The board also contains four W25Q128JVSIQ flash chips, providing 16Mb of memory each. These are for storing network history while the rocket is in flight, which is then written to a microSD on touchdown. A MicroUSB port and JTAG connector are also available for connectivity.

The CAN Gateway is a common node on the Ground System and Launch Vehicle CAN buses. During ground operations, it facilitates bi-directional communication across the two separate networks. Once a message is received in a reception FIFO queue, the interrupt-triggered callback function is immediately called, re-transmitting the frame with a higher priority CAN ID. This combination of higher priority IDs and configuration of interrupts prevents any buffer overflow/ data loss. During flight, the 'gateway' aspect is terminated, and the board acts as a data logger for the Launch Vehicle. This board also monitors the heartbeat of all other connected boards, recording offline if an interval greater than the specified maximum threshold has elapsed since the last time a message originating from a node has been detected. This threshold has provisionally been set to 1 second. All data logged is initially stored to flash chips, then transferred to an SD card after parachute deployment.

## 7.4 Software Overview

### 7.4.1 RTOS and DMA

Both RTOS (Real-Time Operating System) and DMA (Direct Memory Access) are technologies that attempt to ensure the processor can execute critical transactions as much as required, without being blocked by other processes.

DMA delegates the transmission or reception of data over a bus to a dedicated hardware controller that utilises different ‘streams’ to transmit data directly from or to a buffer in memory. This frees up the processor to execute other tasks. The use of interrupts allows customisation of what occurs before the read or write begins and once it has finished.

RTOS allows an MCU’s tasks to be scheduled and executed at a set frequency. Priority is assigned to each task, preventing critical processes from being blocked by non-critical ones. However, not all boards will find ROTS beneficial, particularly boards with fewer distinct or blocking processes. Decisions are being made on a board-by-board basis regarding its use.

### 7.4.2 CAN Bus

The CAN bus allows transfer of commands and data between boards inside the rocket. The CAN protocol was selected due to its robust error checking and priority-based arbitration as well as the good noise immunity provided by differential signalling. Each SRAD board includes the MCP2562 CAN transceiver that develops each board into a respective node on the bus. Termination resistors are placed on the CAN gateway and LoRa boards, which are the lowest and highest physical boards on the stack structure. CAN 2.0B runs at 500 kbit/s, with the bus load inside the rocket running at a 10ms update rate, meaning 5 kbytes is accessible at any point during flight. We calculate the space for at least 30 64-bit messages to be transferable at a 100 Hz update rate. Where each floating-point values accounts for 32-bits. A transfer rate of 60 floating point values is possible every 10ms.

To ensure reliable transmission of data between buses, the CAN gateway was decided to assign each message a high-priority CAN ID which would result in messages being immediately moved from the transmission mailbox to the bus. This was debated against having FIFO-queues that store received messages for processing, or mailboxes that store messages to be transmitted. Careful attention is paid to the assignment of CAN IDs, and prioritisation of different commands on the bus.

### 7.4.3 Memory Management

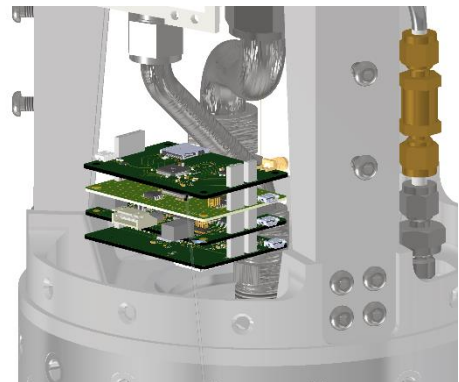
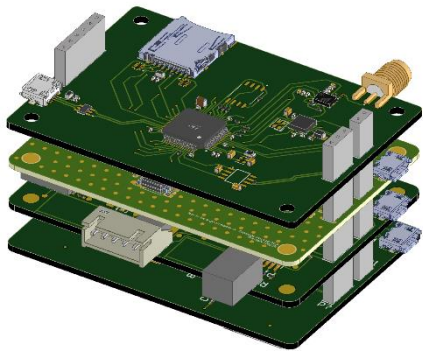
Given the traditional reasons to allocate memory on the heap (such as to store large data-structures) do not apply in this situation, we allocate all memory on the stack. This reduces the overhead associated with memory management and increases the reliability of the system. The exception lies in some of the tools used by the project, namely FreeRTOS, that use the heap extensively. However, they conduct their own memory management.

The 16MB W24Q128JV flash memory was selected as the primary storage medium for data collected throughout the flight. It was chosen over other devices such as SD cards as it does not rely on pad contacts which could be distorted by vibrations during launch. However, as the data from SD cards is easier to extract, some boards contain an SD card and then transfer data from flash to the card after the parachute is deployed and there is more certainty in the reliability of the contact. The sample rate will vary throughout flight to increase the precision of data at critical points in the flight. The storage capacity of the flash is a limitation and sample rates will be carefully selected to ensure it is not exceeded.

## 7.5 Avionics Hardware

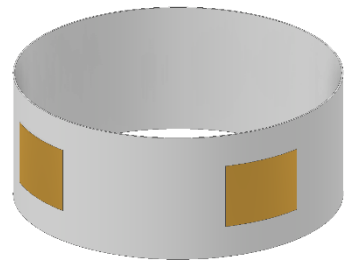
### 7.5.1 Avionics Mounting

Owing to the stack structure, the boards are slotted onto each other and secured using spacers and bolts (not shown). This will ensure that, during flight, vibrations do not cause the boards to lose contact, which would be fatal to the entire system. The example stack-up show in figure x accurately represents the space occupied int eh engine bay, based on last year's CAD model. This design achieves the original objective of creating a robust board structure that optimizes space utilisation and minimises wiring.



### 7.5.2 RF system

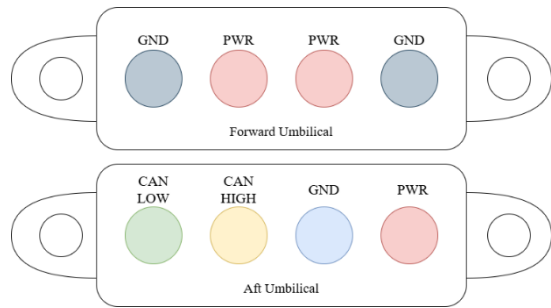
The CATS Vega and LoRa board both operate on a frequency of 2.4 GHz. The antennas used are standard Moxon antenna. These boards will be mounted within the glass fibre tube, and so will have a 360-degree window. The Flight Computer will run on a separate frequency of 868/915 MHz, and will use external patch antennas mounted on the skin, positioned to give an omnidirectional radiation pattern.



Component	Antenna Type	Frequency	Use
CATS Vega	ExpressLRS Moxon	2.4 GHz	LoRa Transmission
CATS Vega	APAE1575R1820ABDC1-T Patch	1.575 GHz	Receive GNSS
LoRa board	ExpressLRS Moxon	2.4 GHz	LoRa Communication
Flight Computer	Patch ring antenna	868/915 MHz	LoRa Communication
Flight Computer	Patch	1.575 GHz	Receive GNSS

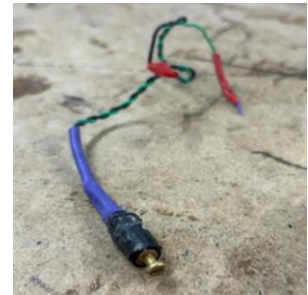
### 7.5.3 Umbilical Connection

The umbilical connection provides power and a CAN to the launch vehicle while in ground operation. These connections are based on 4-pin magnetic pogo pin connectors. The aft umbilical provides power and CAN to the aft stack for the gateway. The forward umbilical only provides power. Power is supplied at 18V from the ground station and is fed into the charging boards. Each pin is rated for 4A, allowing up to 8A of power to flow through a single connector. This high current budget allows for simultaneous charging and reliable valve operation.



### 7.5.4 Arming Switches

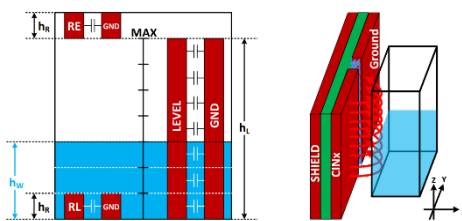
Traditionally, arming switches have been employed using screw-switches. These switches are wired in parallel with the flight computers, and in series with cameras and other systems. Screw-switches require a hole to be drilled into the airframe, to arm the electronics when the launch vehicle is fully assembled. This has disadvantages such as weakening the structure of the composite skin and is also difficult to arm in the field.



An alternative method of arming is being explored, around the technology of using magnetic switches. This requires no holes to be drilled in the airframe, ensuring that the rocket is not affected structurally or aerodynamically. Magnetic switches are unaffected by material properties, since magnetic fields are not noticeably attenuated by carbon fibre. Further design reviews and testing of the switches will be required before flight. In line with the development plan, the magnetic switch will be ready for a test flight on the April subscale launch.

### 7.5.5 Capacitive Level Tank Sensing

There are two main methods of creating a capacitor for Capacitive Level Tank Sensing (CLTS), through concentric tubes or conductive stripes. These copper parts are typically placed within the tank, and as the fuel fills, the permittivity between the copper strips changes, which in turns changes the capacitance reading. A Texas Instruments application paper suggests applying capacitive strips on the outside of a tank and using the fringing capacitance between a primary electrode and ground to determine the level of the liquid inside the tank will also successfully measure the liquid level within the tank. Further tests are required to validate the paper and determine whether curvature or material changes affect the fringing capacitance. (insert reference for the paper)



# Payload

## Overview

The payload is a folding quadcopter designed for deployment from the rocket at apogee. Its primary objective is to follow the rocket's path and collect atmospheric data readings throughout its descent. The quadcopter will autonomously navigate a controlled descent using onboard sensors and waypoints generated based on the tracked rocket flight path to intercept the rocket's exhaust plume. By capturing real-time atmospheric data, it will provide valuable insights into atmospheric conditions, and how rocket emissions may affect them. The collected data will contribute to scientific research and enhance understanding of atmospheric dynamics at high altitudes. Additionally, the quadcopter is engineered to stabilize itself upon release and execute a precise landing at a designated location, ensuring successful data retrieval.

## Project Timeline

Phase	Start	End	Description
<i>1: Designing and manufacturing vehicle</i>	20 <sup>th</sup> January	28 <sup>th</sup> March	<ul style="list-style-type: none"> <li>- Preliminary CAD designs</li> <li>- Developing prototypes using cost effective materials and rapid manufacturing methods such as 3D printing and laser cutting</li> </ul>
<i>2: Developing electronic systems on test drone platform</i>	20 <sup>th</sup> January	28 <sup>th</sup> March	<ul style="list-style-type: none"> <li>- Testing electronics on a test drone frame platform while main vehicle is developed in parallel</li> <li>- Simulate flight plan and adjusting control variables</li> </ul>
<i>3: Ejection mechanism R&amp;D</i>	5 <sup>th</sup> January	28 <sup>th</sup> May	<ul style="list-style-type: none"> <li>- Development of ejection mechanism with collaboration with the electronics and launch vehicle teams</li> </ul>
<i>4: Manufacture and build</i>	10 <sup>th</sup> April	28 <sup>th</sup> April	<ul style="list-style-type: none"> <li>- Manufacturing of finalised model using composite materials, high strength plastic 3D printing and machined fixtures</li> <li>- Integrating electronics</li> </ul>
<i>5: Drop testing</i>	2 <sup>nd</sup> June	20 <sup>th</sup> June	<ul style="list-style-type: none"> <li>- Elevate payload to various altitudes using a cargo drone</li> <li>- Testing ejection mechanism and waypoint tracking</li> </ul>

## Design and Structure

The payload consists of a frame with a carbon fibre base and top plate, a central carbon fibre rod, and 3D-printed and machined fixtures. A composite shell encloses the structure. The propeller arms deploy using a sliding mechanism that reels in a wire, pulling the centre rod mounted slider down until it engages with a locking mechanism. The quadcopter is bottom-heavy to enable self-stabilization, and its droplet-shaped design assists in descent control. The total weight of the payload is approximately 1.2kg.

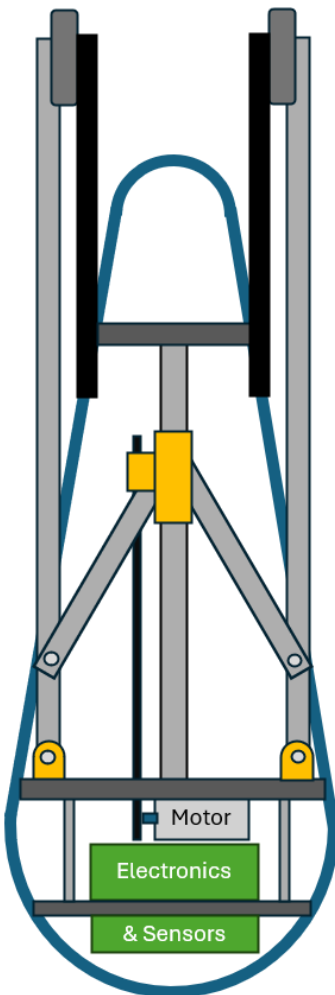


*Figure 1: Cross-sectional diagram of payload structured in folded state*

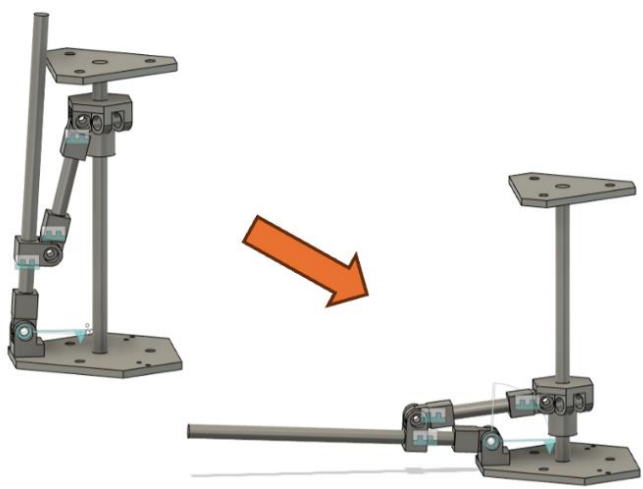


*Figure 2: Side view of prop arm folding mechanism*

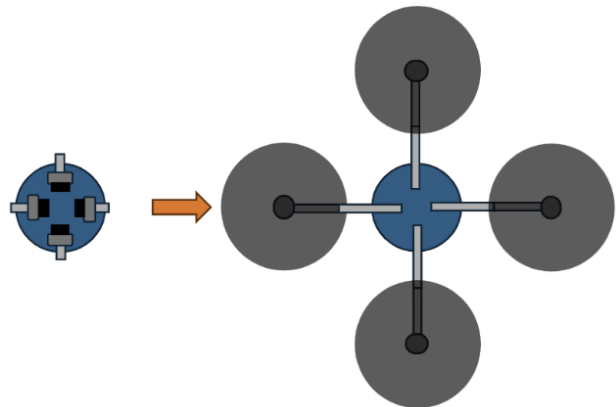


*Figure 3: Top view of payload in folded and unfolded state*

## Flight Controller

The payload is equipped with an Orange Cube + Mini flight controller running ArduPilot firmware. The Orange Cube will also house key navigation sensors, including position (GPS), orientation (onboard compass and gyroscope), and an onboard barometer to provide altitude data. During launch, the Orange Cube will begin operation, collecting real-time location data retrieved from the launch vehicle. This allows precise GPS tracking without interference by the outer shell of the rocket, ensuring the drone can accurately stabilize and navigate through the fumes of the rocket. This system provides real-time navigation, stabilization, and flight control functions, ensuring autonomous waypoint tracking and controlled descent. Additionally, a Raspberry Pi Zero is integrated into the system to handle flight waypoints and deployment sequences, allowing for optimized descent planning.

3

## Telemetry and Tracking

The payload utilizes a GPS tracker for continuous position tracking during descent and recovery. This ensures that the flight path is accurately recorded and facilitates post-mission retrieval of the

payload. An onboard data logger is responsible for capturing flight telemetry, including altitude, velocity, and atmospheric data throughout the descent. This recorded information is essential for post-flight analysis, allowing for assessment of the quadcopter's performance and environmental conditions during the mission. The combination of real-time GPS tracking and onboard data logging ensures comprehensive telemetry collection, supporting both real-time monitoring and scientific research objectives.

## Flight Stages

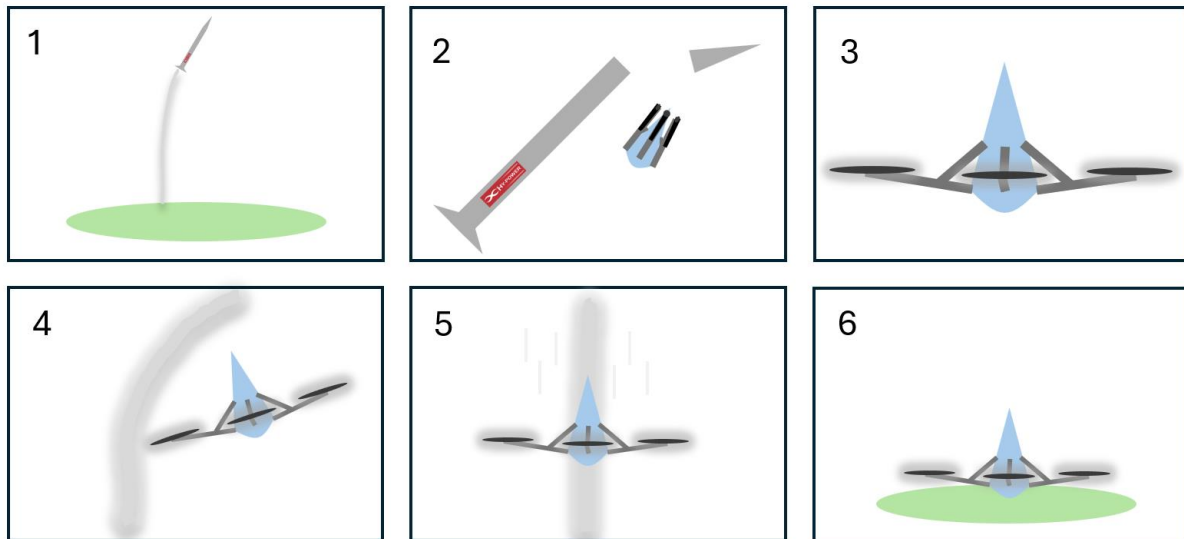


Figure 4: Illustration of the flight stages

First, the rocket climbs to an altitude of 3 km while the payload continuously tracks its path using GPS data provided by the rocket. Upon reaching the 3 KM target apogee, the rocket ejects the payload from the nose cone using pressurized gas to ensure a clean separation. After the payload is clear of conflict with the rocket. Once safely separated, its propeller arms unfold (*using the hinge mechanism in Figure 2*), marking the start of the flight sequence. It then follows predefined waypoints, automatically skipping any missed waypoints due to wind or speed variations. During controlled descent, its descent rate is carefully managed to maintain stability while collecting atmospheric data from the fumes of the rocket. As it nears the ground, the payload gradually reduces speed before landing safely in a designated area.

## Key flight stages

### 1. Rocket Launch and Ascension

- Rocket climbs to an altitude of 3km
- Payload tracks the path using GPS

### 2. Payload Ejection

- At 3 km altitude (target rocket apogee), the rocket releases the payload from the cone
- Pressurised gas is used to separate the structures

### 3. Unfolding sequence

- Payload self-aligns passively due to its geometry

- The prop arms unfold, and the flight sequence starts

#### 4. Following Waypoints

- Payload follows predefined waypoints.
- If a waypoint is missed due to speed or wind, it skips to the next automatically.

#### 5. Controlled Descent

- The descent rate is limited to maintain stability.
- Atmospheric data readings are collected throughout the descent.

#### 6. Landing Process

- Payload reduces speed as it nears the ground.
- Payload lands in a predefined safe landing area

## Testing and Validation

To ensure the reliability of the payload's flight and descent systems, both simulation and real-world testing will be conducted. Software testing will be carried out using ArduPilot SITL. This allows for the validation of waypoint logic and descent parameters in a controlled virtual environment. Once the software is refined, real-world testing will involve lifting and releasing the payload from various altitudes using a heavy-duty drone. These tests will focus on key aspects such as deployment mechanism, waypoint tracking accuracy, and landing precision, ensuring that the payload performs as expected under real flight conditions.

## Key Considerations

Key considerations for the payload's performance and reliability include air density impact, failsafe mechanisms, and post-mission analysis. At high altitudes, lower air density can affect motor lift capacity and propeller efficiency, which requires optimization to ensure stable flight and controlled descent. Failsafe mechanisms, such as battery monitoring, GPS tracking, emergency chute, and altitude-based triggers, will be implemented to guarantee a safe descent in case of system failures. After each mission, a detailed log analysis will be held to assess descent rate, waypoint transitions, and battery usage, providing valuable insights for further optimization. Additionally, a GPS tracker will be used to aid in the payload's recovery, ensuring data retrieval and mission success.

## Conclusion

The folding quadcopter is designed for high-altitude deployment, controlled descent, and autonomous landing. The combination of simulations, incremental testing, and system configurations ensures mission reliability and success while collecting atmospheric data during descent.

**4 Pages for Payload**

## 9. Conclusions and Outlook

## 10. Appendices

If you would like to include engineering drawings, schematics, test plans or test results, please use the appendices to do so.

Table 3 Specific Impulse Efficiency - O/F = 1.9

INJECTOR	$P_c$ PSIA	% Si			
		0	0.5	1.0	2.0
FUEL BARRIER	500	90.6	90.7	90.6	89.5
	750	92.4	92.5	92.3	91.5
	1000	93.4	93.3	93.1	92.1
FUEL/OX BARRIER	500	91.4	92.0	92.4	91.9
	750	92.8	93.0	93.5	93.3
	1000	93.7	93.7	94.0	93.4

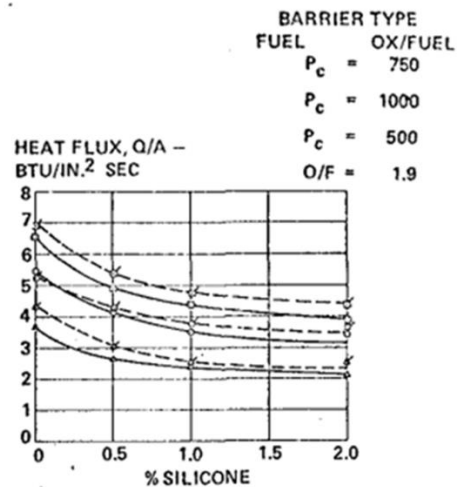


Fig. 11 Convergent Section Heat Transfer

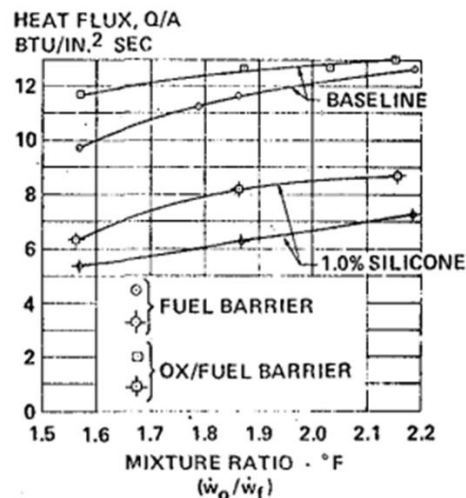


Fig. 9 Throat Section Heat Transfer -  $P_c = 750$  psia

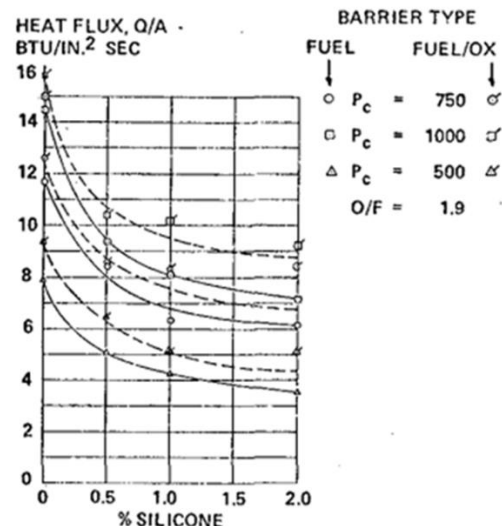


Fig. 12 Throat Section Heat Transfer

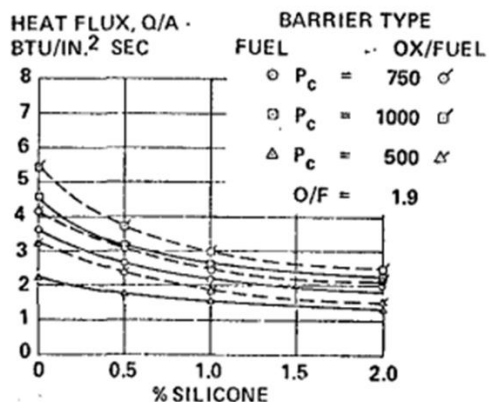


Fig. 10 Chamber Section Heat Transfer

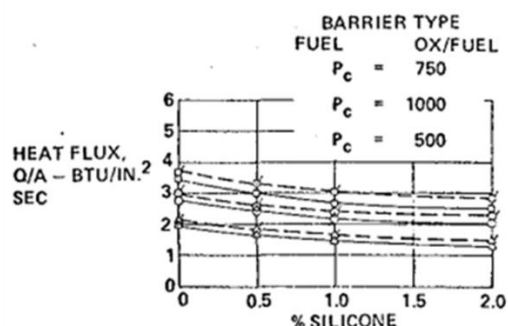


Fig. 13 Divergent Section Heat Transfer

Figure 42: Combustion Chamber - PDMS performance and total heat flux reduction figures

## Fuelling operations

Check Number		Asset	Fuelling sequence
Date		Sub Team	Ground Station
Items to be checked		Acceptance Criteria	
List the action required to be performed		List the required outcome to pass the check	
1.0	Action	Acceptance	Checker      Observer
1.1	Open Ethanol fuel tank vent and fuelling valve	Visual on open valves	
1.2	Insert fluid pump and begin pumping		
1.3	Monitor ethanol reservoir tank weight		
1.4	Stop manual pump when weight is reached	4.5l	
1.5	Close ethanol vent valve		
1.6	Close ethanol fill valve		
2.0	Action	Acceptance	Checker      Observer
2.1	Ensure N2O <del>Pressurant</del> valve is closed		
2.2	Open N2 fuelling valve		
2.3	Monitor N2 tank fuelling status		
2.4	Close N2 fuelling valve when desired pressure reached	300 bar	
3.0	Action	Acceptance	Checker      Observer
3.1	Ensure N2O vent valve closed		
3.2	Open N2O fuelling valve		
3.3	Monitor N2O tank fuelling status		
3.4	Open N2O vent valve and continue filling		
3.4	Close N2O fuelling valve and N2O vent valve as N2O reaches outtake tube level.	50 bar 13l Visual plume from vent.	
3.5	Open N2O <del>pressurant</del> Valve	Pressure Stabilises at 50-55 bar	
Final Validation (Team Member Signature)			
Total of Inspections Satisfactory / Not Satisfactory			

Figure 43 Fuelling operations checklist

## References

- [1] '(PDF) Silicon Oil Thermal Barrier System for in Space Applications', in *ResearchGate*, doi: 10.13140/RG.2.1.2230.3601.
- [2] H. Loftus, L. Montanino, L. Nasiak, and C. Schmidt, 'Additives for heat flux reduction', in *9th Propulsion Conference*, in Joint Propulsion Conferences., American Institute of Aeronautics and Astronautics, 1973. doi: 10.2514/6.1973-1289.

## References

Bayvel, L. a. (2019). *Liquid atomization*. Abingdon: Routledge.

Bazarov, V. Y. (2004). Design and dynamics of jet and swirl injectors. In *Liquid rocket thrust chambers: aspects of modeling, analysis, and design* (pp. 19-103). Reston, VA: AIAA.

NASA. (1976). *Liquid rocket engine injectors - NASA SP-8089*. Cleveland, Ohio: NASA.

Zimmerman, J. &. (2013). Review and Evaluation of Models for Self-Pressurizing Propellant Tank Dynamics. *Zimmerman, Jonah & Waxman, Benjamin & Cantwell, Brian & Zilliac, Gregory. (2013)49th AIAA/ASME/SAE/ASEE Joint Propulsion Conference.*

[1] Bayvel, L.P. and Orzechowski, Z. (2019) Liquid atomization. Abingdon: Routledge.

[2] Bazarov, V., Yang, V., and Puri, P.B. (2004) 'Design and dynamics of jet and swirl injectors', in Yang, V., Habiballah, M., Hulka, J., and Popp, M. (eds.) *Liquid rocket thrust chambers: aspects of modeling, analysis, and design*. Reston, VA: AIAA, pp. 19–103.